JAMES | Journal of Advances in Modeling Earth Systems

RESEARCH ARTICLE
10.1029/2022MS003200

Key Points:

- Partially coupled (PCPL) models are able to simulate ocean-atmosphere feedbacks necessary to maintain a stable Atlantic Meridional Overturning Circulation (AMOC)
- AMOC variability in PCPL experiments is significantly correlated to forced ocean models on timescales below 5 years and at all latitudes
- Wind stress curl contributions to decadal AMOC variability can be reproduced in PCPL, while the buoyancy contribution cannot

Supporting Information:

Supporting Information may be found in the online version of this article.

Correspondence to:

T. Schulzki,
tschulzki@geomar.de

Citation:

Schulzki, T., Harlaß, J., Schwarzkopf, F. U., & Biastoch, A. (2022). Toward ocean hindcasts in earth system models: AMOC variability in a partially coupled model at eddying resolution. *Journal of Advances in Modeling Earth Systems*, *14*, e2022MS003200. https://doi.org/10.1029/2022MS003200

Received 19 MAY 2022
Accepted 1 DEC 2022

Author Contributions:

Conceptualization: Tobias Schulzki, Arne Biastoch
Formal analysis: Tobias Schulzki
Funding acquisition: Arne Biastoch
Methodology: Tobias Schulzki, Jan Harlaß, Franziska U. Schwarzkopf
Project Administration: Arne Biastoch
Software: Tobias Schulzki, Jan Harlaß, Franziska U. Schwarzkopf
Supervision: Arne Biastoch

Toward Ocean Hindcasts in Earth System Models: AMOC Variability in a Partially Coupled Model at Eddying Resolution

Tobias Schulzki[1], Jan Harlaß[1], Franziska U. Schwarzkopf[1], and Arne Biastoch[1,2]

[1]GEOMAR Helmholtz Centre for Ocean Research Kiel, Kiel, Germany, [2]Christian-Albrechts Universität zu Kiel, Kiel, Germany

Abstract While forced ocean hindcast simulations are useful for a wide range of applications, a key limitation is their inability to simulate ocean-atmosphere feedbacks. As a consequence, they need to rely on artificial choices such as sea surface salinity restoring and other corrections affecting the surface freshwater fluxes. Fully coupled models overcome these limitations, but lack the correct timing of variability due to weaker observational constraints. This leads to a mismatch between forced and coupled models on interannual to decadal timescales. A possibility to combine the advantages of both modeling strategies is to apply a partial coupling (PCPL), that is, replacing the surface winds stress in the ocean component by wind stress derived from reanalysis. To identify the capabilities, limitations and possible use cases of partial coupling, we perform a fully coupled, two partially coupled and an ocean-only experiment using an all-Atlantic nested ocean configuration at eddying resolution in a global climate model. We show that the correct timing of Atlantic Meridional Overturning Circulation (AMOC) variability in PCPL experiments is robust on timescales below 5 years. Mid-latitude wind stress curl changes contribute to decadal AMOC variability, but North Atlantic buoyancy fluxes are not significantly altered by incorporating reanalyzed wind stress anomalies, limiting the success of PCPL on this timescale. Long term trends of the AMOC in PCPL mode are consistent with fully coupled model experiments under historic atmospheric boundary conditions, suggesting that a partially coupled model is still able to simulate the important ocean-atmosphere feedbacks necessary to maintain a stable AMOC.

Plain Language Summary The Atlantic Meridional Overturning Circulation (AMOC) is one of the most important quantities characterizing the circulation in the Atlantic Ocean and influences the climate in its surrounding countries. It is traditionally simulated with forced ocean-only or coupled ocean-atmosphere models. In this study we force the ocean component of a coupled climate model with observed wind stress anomalies, aiming to combine the advantages of these two most often applied modeling strategies, while omitting their respective key limitations. This can ultimately lead to an improved representation of the AMOC in models, a prerequisite to understand past and future changes of this complex circulation system. Furthermore, our set of model experiments directly isolates the role of wind variability on various timescales and different latitudes, improving our knowledge of processes generating changes in the AMOC.

1. Introduction

Owing to its major importance for the ocean heat transport and thus climate variability, the Atlantic Meridional Overturning Circulation (AMOC) has been a focus of study for several decades (Lozier, 2012). Still today, the complex AMOC is not fully understood in terms of strength, meridional coherence, drivers of long term changes and many other aspects. The existence of strong variability on interannual and decadal timescales makes the detection and attribution of potential recent AMOC changes challenging (Jackson et al., 2022). Direct observations for at least several decades would be needed to infer long term trends and their drivers. A detailed knowledge of mechanisms determining the past AMOC evolution is particularly important to assess future risks in the light of climate change, with models projecting a weakening of the AMOC until the end of this century (Weijer et al., 2020).

In addition to direct (yet sparse) observations by mooring arrays in the North and South Atlantic, numerical models largely contribute to our understanding of past AMOC variability. One of the most frequently used model set-ups are ocean general circulation models (OGCMs) forced with momentum, heat and freshwater fluxes derived from a prescribed atmospheric state based on reanalysis products, using bulk formulae, and thus incorporating observa-

Visualization: Tobias Schulzki
Writing – original draft: Tobias Schulzki
Writing – review & editing: Tobias Schulzki, Jan Harlaß, Franziska U. Schwarzkopf, Arne Biastoch

tions (Griffies et al., 2009; Tsujino et al., 2018). As a result, they are typically able to capture the observed timing of AMOC variability on various timescales (Roberts et al., 2013). A major disadvantage of forced (ocean-only) model simulations, however, is that prescribing the atmospheric state leaves very limited ability of the oceanic evolution to feed back to the atmospheric forcing (only through the bulk formulae's dependency on the ocean state). As a consequence, they typically act overly sensitive to freshwater forcing and require the application of sea-surface salinity (SSS) restoring terms (Griffies et al., 2009; Rahmstorf & Willebrand, 1995). This restoring term has an arbitrary strength and is not based on physical laws, nor empirical equations. Additionally, the global freshwater budget is not closed in such a model set-up (Griffies et al., 2009). Even if budget corrections are applied, they involve a redistribution of freshwater with horizontal patterns that are not expected to be realistic. Especially multidecadal trends and decadal variability of the AMOC were shown to be highly sensitive to restoring and budget correction choices (Behrens et al., 2013; Biastoch et al., 2021).

However, models are not limited to the ocean and OGCMs can be embedded in earth system models (ESMs) that simulate the interaction of several components of the climate system. These coupled models allow to explicitly simulate ocean-atmosphere feedbacks, therefore SSS restoring is not necessary. Also, energy and freshwater budgets are (nearly) closed without the need for artificial corrections. In contrast to forced OGCMs, ESMs only incorporate observations via atmospheric boundary conditions such as trace gas concentrations and land use changes. Variability of climate indices like ENSO, but also variability of the ocean circulation (e.g., AMOC), are generated internally in the coupled model. While the magnitude and/or period of this variability can be in agreement with observations, the timing of variability (e.g., years of maximum/minimum AMOC transport) is not (Cheng et al., 2013; Ding et al., 2013; Flato et al., 2013). Especially for sensitivity experiments with changes to one model parameter, or variable (e.g., increased CO_2 concentration), internally generated variability with unknown timing makes the attribution of changes more difficult. As a consequence, many scientific questions can only be addressed statistically in ensemble experiments.

An attempt to combine the advantages of the two modeling strategies is to apply a partial coupling (PCPL; Ding et al., 2013). Here, surface heat and freshwater fluxes are exchanged between the ocean and atmosphere model, as done in a fully coupled ESM. The wind stress (or momentum flux) on the other hand is calculated from reanalyzed wind, replacing the wind stress that would otherwise be provided from the atmospheric to the oceanic component of the model. Thoma et al. (2015) showed that PCPL can improve the timing of historical climate fluctuations, especially in the Pacific. Even multidecadal variability, namely the Pacific Decadal Oscillation (PDO), is simulated with improved timing. Additionally, their partially coupled model is also able to reproduce interannual variations of the AMOC as observed at 26.5°N. This result is in line with various studies showing that interannual AMOC variations at this latitude are mostly attributable to wind forcing (Biastoch et al., 2008; Zhao & Johns, 2014). Still, it is not clear whether partial coupling is similarly successful at other latitudes, since AMOC variability at different latitudes can have strongly different characteristics (e.g., Blaker et al., 2021; Jackson et al., 2022). Furthermore, AMOC variability in the South Atlantic was shown to have a significant contribution from intrinsic (un-forced) variability and is thus less tied to the applied (wind stress) forcing (Grégorio et al., 2015; Leroux et al., 2018). Thoma et al. (2015) only studied AMOC variability on interannual timescales and the question remains, whether PCPL experiments and observations (or ocean-only models) are also correlated on shorter and longer (decadal) timescales.

Partial coupling has the potential to improve the representation of the AMOC in hindcast simulations by combining the advantages of coupled and ocean-only simulations. Following Danabasoglu et al. (2014) the term 'hindcast' is used here to describe forced OGCM simulations with the goal to reproduce the past climate and should not be confused with initialized forecasts of the past (also called hindcast, e.g., Reintges et al. (2020)). Even if partial coupling may not be an alternative to coupled and forced simulations, it could provide a valuable set-up for sensitivity experiments with more specific questions. Although Thoma et al. (2015) provide a comprehensive analysis of variability in partially coupled experiments, several important characteristics of such simulations are currently unknown. In particular, this includes possible spatial and temporal limitations to reproduce past AMOC variability. Therefore, it is not yet possible to decide for which scientific questions partial coupling can be an advantageous alternative to forced or fully coupled model experiments and to envision possible improvements of the procedure.

Here, our aim is to provide a detailed description of the technical implementation of partial coupling in a high-resolution coupled model and to study its capability to reproduce the past ocean circulation (variability).

Although our focus is on the AMOC transport, the AMOC is an integrative measure and thus incorporates various circulation systems. We also study the impact of partial coupling on the basin-scale horizontal gyres, which dominate the large-scale circulation in the horizontal plane and may be even more directly influenced by the applied wind stress forcing. The motivation for this study and our main goals can be summarized by the following questions:

- Does a partially coupled ESM reproduce the observed large-scale ocean circulation, including its timing of variability? Specifically:
  – Do PCPL experiments simulate a realistic mean large-scale circulation and multi-decadal trends?
  – Is the correct timing of (AMOC) variability in PCPL experiments limited to certain latitudes, or timescales?

Our analysis is based on the comparison of fully coupled, partially coupled and forced (ocean-only) model experiments. All experiments were performed with a global nested configuration covering the whole Atlantic Ocean at an eddying resolution of 1/10°. This resolution includes an important range of variability, since the presence of eddies throughout large areas of the Atlantic Ocean and their importance was shown in many studies (e.g., Chelton et al., 2011; Hallberg & Gnanadesikan, 2006; Rieck et al., 2019). Several aspects of the large-scale circulation and its variability were shown to improve with a higher horizontal resolution, including the gyre circulation and AMOC (Hirschi et al., 2020). A better representation of the mesoscale is thus expected to cause a more realistic response to the applied surface forcing, but also introduce more variability into individual current components (Biastoch et al., 2021).

First, we provide a detailed description of the model configuration, implementation of partial coupling and the applied surface momentum and buoyancy forcing in Section 2. We then show how partial coupling affects the mean large-scale circulation, as well as its variability and long term evolution in Section 3. Section 4 contains an in-depth analysis of the timing of variability in partially coupled simulations with a strong focus on the AMOC.

2. Model and Methods

In this study, we employ the flexible ocean and climate infrastructure (FOCI), a coupled ocean-atmosphere-land model (Matthes et al., 2020), capable of including high-resolution ocean nests, to perform a series of model experiments. We here utilize a coupled (FOCI-ATLAS10) and an un-coupled (ATLAS10) configuration with an eddying Atlantic Ocean. In the following we describe the coupled configuration and the implementation of partial coupling. Afterward we describe the un-coupled (ocean-only) configuration and analyze the wind stress, heat and freshwater fluxes driving the ocean component in the different experiments.

2.1. Coupled Configuration: FOCI-ATLAS10

The ocean component of the coupled model is based on the Nucleus for European Modeling of the Ocean (NEMO) version 3.6, ocean sea-ice model (Madec, 2016). The Louvain-la-Neuve Sea Ice Model version 2 (LIM2; Fichefet & Maqueda, 1997; Vancoppenolle et al., 2009) is used as the sea-ice component.

ATLAS10 consists of a global grid (hereafter referred to as host) with a therein embedded, so called, nest with increased grid resolution. The host has a horizontal resolution of 0.5° on a tripolar Arakawa C-grid and 46 z-levels with increasing grid spacing from 6 m at the surface to 250 m at depth with application of partial cells at the seafloor (ORCA05 configuration; Barnier et al., 2006; Biastoch et al., 2008).

The nested area covers the Atlantic Ocean from 99°W to 62°E and from 65°S to approximately 65°N (Figure 1). Within the nest, the horizontal resolution is increased to 1/10°. This corresponds to a grid spacing of ∼5 km at high latitudes and 11 km in the tropics. Along with the higher horizontal resolution, the time step on the nest grid is reduced by a factor of 3 to ensure the CFL criterion is fulfilled. The vertical axis is unchanged compared to the host. The nest bathymetry is obtained by interpolating the ETOPO1 data set (Amante & Eakins, 2009) onto the model grid using the nesting tools (Lemarié, 2006). Thereby, also an updated bathymetry for the host is generated, where coastlines are adjusted, assuring grid cells on the host grid communicating to ocean cells on the nest grid, are also represented as ocean cells. However, in our coupled simulations, due to the coupling procedure itself (see below), the standard ORCA05 coastline is used in the host to avoid inconsistencies between the ocean's and the atmosphere's land-sea masks.

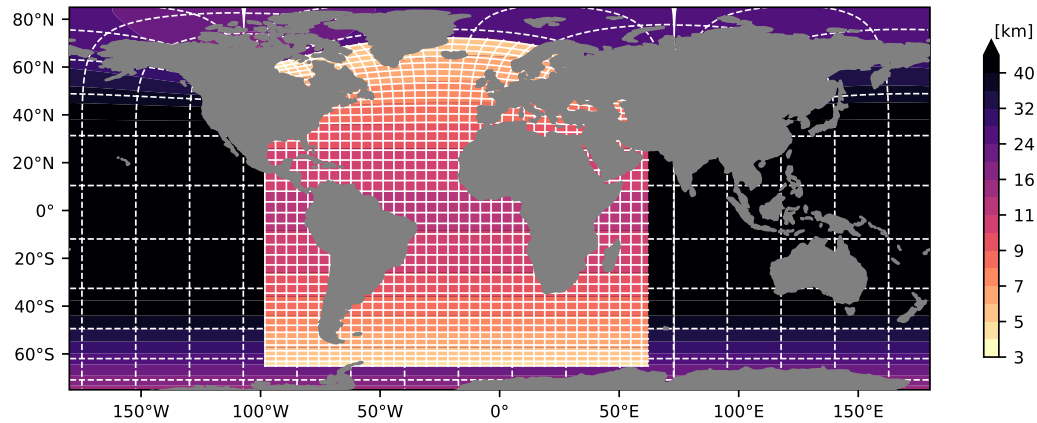

Figure 1. Visualization of the oceanic grid in the ATLAS10 nested configuration. Color shading shows the zonal distance between grid points. Every 45th grid line of the nest and host is shown.

Exchange between the nest and host is accomplished by 2-way Adaptive Grid Refinement in Fortran (Debreu et al., 2008). The global host not only provides lateral boundary conditions for the nest, but information is also fed back to the host at every time step along the nest boundary. After a given number of such cycles, the host is updated with the nest solution inside the full 3-dimensional domain covered by the nest (baroclinic update). This also holds for the sea-ice component which is integrated on both, the nest and the host grid. The lateral boundary of the nest involves a 6 nest grid point wide sponge layer to damp outgoing flow features that are smaller than resolved by the coarse host grid. We use a sponge layer coefficient of 3,000 $m^2\ s^{-1}$. While free-slip lateral momentum boundary conditions are used on the host grid, no-slip is used in the nest, mostly due to slightly more realistic/enhanced mesoscale variability in key regions as the Labrador Sea or Mozambique Channel (see also Quartly et al., 2013; Rieck et al., 2019; Schwarzkopf et al., 2019). However, it should be mentioned that overall no-slip boundary conditions perform less well in the northern than in the southern hemisphere. Especially the North Atlantic Current (NAC) path is less realistic (compare Penduff et al. (2007)).

On both model grids the vertical eddy viscosity and diffusivity coefficients are derived from a turbulent kinetic energy model (TKE; Blanke & Delecluse, 1993; Bougeault & Lacarrere, 1989).

In the non-eddying host we use the Total Variance Dissipation (TVD; Zalesak, 1979) scheme for tracer advection with a Laplacian diffusion operator acting along iso-neutral surfaces with an eddy diffusivity of 600 $m^2\ s^{-1}$. Further, we apply a Gent and McWilliams (GM) eddy parameterization (Gent & Mcwilliams, 1990) with an eddy induced velocity coefficient of 1,000 $m^2\ s^{-1}$. Lateral advection of momentum is represented in vector invariant form, where the vorticity term is solved using the energy and enstrophy conserving (EEN; Arakawa & Hsu, 1990) scheme. Lateral diffusion of momentum is accomplished by a bi-Laplacian operator acting along geopotential surfaces with a maximum eddy viscosity of $6 \times 10^{11}\ m^4\ s^{-1}$.

In the eddying nest, the tracer and momentum advection equations are solved using the self-diffusive upstream-biased scheme (UBS; Farrow & Stevens, 1995; Madec, 2016). No additional explicit diffusion terms were used in the advection equations. The UBS scheme was chosen, as it was found to perform similar to the TVD/EEN advection schemes (used on the host grid) in the coupled configuration, but with a slightly better representation of eddy activity (higher, more realistic, SSH variance and EKE) in many regions.

Surface boundary conditions for FOCI-ATLAS10's ocean component are derived from interactive atmosphere and land models. The atmospheric component of FOCI is provided by ECHAM6 (Müller et al., 2018; Stevens et al., 2013) with 96 vertical levels and a spectral resolution of T63 (~200 km) in the horizontal plane. Albedo, soil moisture, snow cover, leaf area and vegetation distribution are interactively simulated by the JSBACH land model (Brovkin et al., 2009; Reick et al., 2013).

Surface boundary conditions are calculated in ECHAM6 and provided to the host grid via the OASIS3-MCT coupler (Valcke, 2013). These include solar and non-solar heat fluxes, freshwater fluxes and wind stress. The wind stress calculation includes ocean current feedbacks ("relative wind"). A direct exchange between the ocean nest and atmosphere is currently not implemented, consequently, only the host grid is directly coupled to

ECHAM6 (every 3 hr), while the nest grid receives the same atmospheric state as boundary conditions every 30 min (constant for 3 hr) interpolated onto its oceanic grid. The nest itself feeds back its baroclinic solution onto the host grid every third host grid time step (90 min), thereby indirectly also affecting the atmosphere. The exchange with the sea-ice model takes place every 3 hr on the host and every 30 min on the nest grid.

A fully coupled historical experiment is initialized with atmospheric boundary conditions of the year 1850. The ocean and atmosphere initial states are taken from the end of a 1,500 years long FOCI (un-nested standard configuration) control simulation described in Matthes et al. (2020). To initialize the nest, all restart variables are interpolated from the ORCA05 grid to the ATLAS10 grid. The model is then integrated for 163 years until 2013 under historic atmospheric boundary conditions that follow the CMIP protocol as described in Meinshausen et al. (2017). This experiment will be referred to as FOCI-ATLAS10-CPL (short: CPL) in the following. The first 108 years, regarded as the spin-up, are not analyzed here.

2.2. Partial Coupling

As described above, the ocean component receives surface boundary conditions from the interactive atmosphere in the fully coupled configuration. When using partial coupling the wind stress is no longer calculated by ECHAM6, but derived from reanalyzed 10 m wind fields. The heat and freshwater fluxes still depend on the wind simulated by ECHAM6. In this study we employ the 10 m wind fields provided by the JRA55-do version 1.5 data set (Tsujino et al., 2018) to force the ocean component of FOCI. The 10 m wind is converted to wind stress using bulk formulae (Large & Yeager, 2009). We neglect ocean current feedbacks and derive the wind stress formulated as "absolute winds." We use a constant atmospheric density of 1.22 kg m^{-3} and a drag coefficient that depends on the wind speed according to Large and Yeager (2009). We do not account for atmospheric stability, that is, we use 10 m wind rather than 10 m neutral wind, as the necessary input fields to keep a clean separation between wind stress climatology (purely from the model) and wind stress anomaly (purely from reanalysis) were not available.

Following Thoma et al. (2015), we calculate an anomaly forcing in which the wind stress anomalies are taken from the 3-hourly resolved reanalyzed wind stress interpolated onto the ECHAM6 T63 grid, while the climatology is replaced. To derive the applied wind stress climatology, we employ two different strategies: In a first experiment (FOCI-ATLAS10-PCPL-LOW; short PCPL-L) the monthly climatology of the reanalysis is replaced by the monthly climatology of an un-nested FOCI 3-member ensemble, under a historical forcing based on the years 1850–2013. We use the same procedure to calculate the wind stress climatology in the FOCI ensemble, as for the reanalysis (based on the 10-m wind). As discussed later this results in a lower mean wind stress compared to CPL, but a similar mean wind stress compared to the ocean-only simulation described below. Choosing the 3-member ensemble climatology was based on initial experiments run without the 1/10° ocean nest and then kept for PCPL-L. Differences between the FOCI-ATLAS10-CPL climatology and FOCI (un-nested) ensemble climatologies are overall small, except for a slightly stronger mean wind stress in the North Atlantic in CPL. Because the main purpose of PCPL-L is to investigate, whether the mean wind stress impacts the ability of PCPL to reproduce the timing of AMOC variability, the 3-member ensemble climatology is still suited here. With the second experiment (FOCI-ATLAS10-PCPL-HIGH; short PCPL-H) we are aiming at generating a wind stress forcing as comparable as possible to CPL. Therefore, we replace the reanalysis wind stress climatology by the 1958–2013 climatology derived from CPL. Here we directly use the wind stress calculated and stored by ECHAM6 and do not apply the offline bulk formulae to the 10 m wind.

The wind stress anomaly forcing is provided on the ECHAM6 T63 grid and then interpolated onto the host and nest grids. The wind stress forcing is not interpolated in time, but constant at all model time steps within 3 hr for both, host and nest. A summary of the partial coupling procedure applied here is visualized in Figure 2.

The partially coupled experiments are initialized from the FOCI-ATLAS10-CPL simulation from the last time step on 31 December 1957. Subsequently the model is integrated forward over the length of the atmospheric boundary condition data set (until 2013), resulting in 56 years long model simulations. Apart from the different surface boundary conditions in the ocean component of FOCI, all settings described above are identical for FOCI-ATLAS10-CPL and the two FOCI-ATLAS10-PCPL experiments.

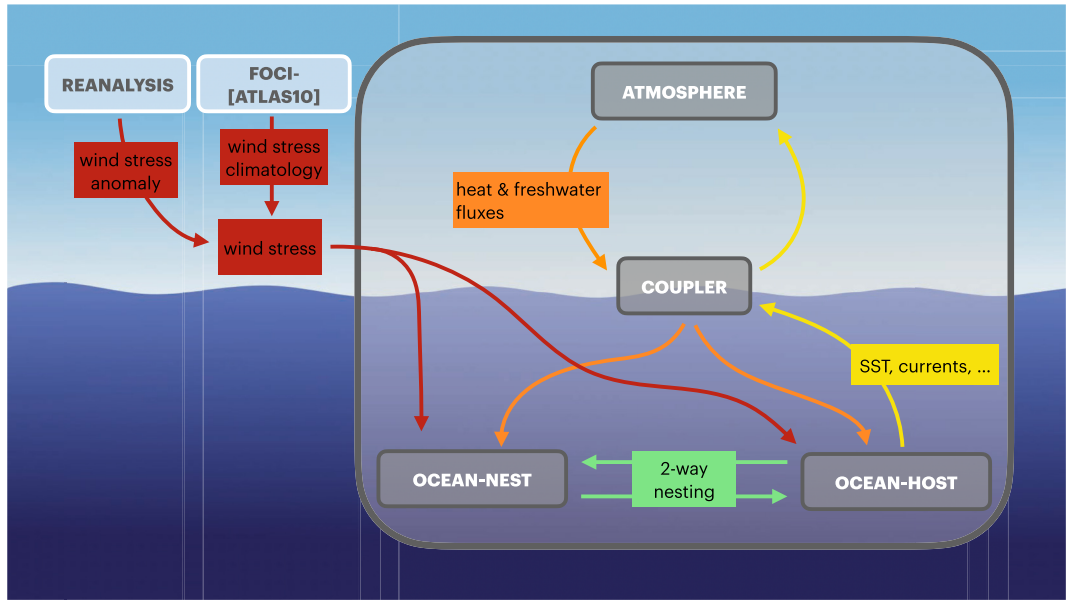

Figure 2. Schematic diagram showing the implementation of partial coupling in the FOCI-ATLAS10 configuration. Components that are part of FOCI and interact during runtime are enclosed in the large gray box. Wind stress is calculated offline and read from disk.

2.3. Ocean-Only Configuration: ATLAS10

Additional to the coupled configuration, we run a forced (ocean-only) experiment using the ocean component of FOCI-ATLAS10. All surface fluxes are derived from the JRA55-do version 1.5 forcing data set. This experiment is referred to as ATLAS10-OCO (short: OCO). During runtime, all variables, except runoff, are interpolated onto the nest and host grids. Surface fluxes are then derived from the forcing data set using bulk formulae (Large & Yeager, 2009). The runoff was first remapped onto the host grid using the procedure of Martin (2021) described in Biastoch et al. (2021) with a search radius of 160 km, but without application of the described river plume scheme. Afterward, the runoff was interpolated onto the nest grid assuring no loss of runoff on land by redistribution to the nearest ocean grid points. Within NEMO, river mouth treatment is activated, increasing vertical mixing within the top 10 m of the water column at every runoff grid point.

As many namelist parameters as possible remain unchanged compared to the (partially) coupled set-ups described above. The main purpose of this experiment is to provide a best estimate of the AMOC variability's timing, in a set-up comparable to our fully and partially coupled experiments. We adopt restoring settings from a successful model simulation of the North Atlantic in the higher resolved VIKING20X model, described in Biastoch et al. (2021): SSS restoring is applied with a piston velocity of 50.0 m yr^{-1} everywhere, excluding ice-covered regions, in grid cells with runoff and additionally within a distance of 80 km around Greenland. Therefore, the freshwater input from rivers and ice-sheet melting is not immediately damped. Also the Mediterranean Sea outflow (below 700 m) is restored to climatological temperature and salinity values using a three dimensional mask with a maximum Newtonian damping coefficient of 6.34×10^{-5} s^{-1}. In an ocean-only experiment the atmospheric forcing is prescribed and the larger ocean area of the updated host bathymetry can be used. Together with the surface boundary conditions, which are calculated simultaneously on the host and the nest grid at every exchange time step (30 min), the full exchange (including baroclinic update) between the two components takes place. A main difference between the ocean-only and FOCI-ATLAS10 configurations is the use of the TVD and EEN advection schemes, not only on the host, but also on the nest grid instead of the UBS scheme. As on the host grid, a Laplacian diffusion operator is added to the tracer advection equation and a bi-Laplacian operator to the momentum advection equation. Eddy diffusivities are adjusted to the higher grid resolution (120 m^2 s^{-1} and 2.4×10^{10} m^4 s^{-1}). The reason for this switch is to achieve a more realistic multi-decadal AMOC trend. The UBS scheme, together with the model settings tuned for the TVD/EEN schemes, did cause the AMOC to considerably decrease over time. Note that this is not the case for the coupled configuration, where UBS does not cause a long term AMOC decline.

Table 1
Overview of Experiments

Experiment	CPL	PCPL-L	PCPL-H	OCO
Mode	CPL	PCPL	PCPL	OCO
Heat/freshwater	ECHAM6	ECHAM6	ECHAM6	JRA55-do
Wind stress anomalies	ECHAM6	JRA55-do	JRA55-do	JRA55-do
Wind stress climatology	ECHAM6	FOCI-Ensemble	CPL	JRA55-do
Forcing resolution	T63 (≈1.9°)	T63 (≈1.9°)	T63 (≈1.9°)	TL319 (0.5625°)
Current feedback	Yes	No	No	Yes
Initialization	FOCI-piCtrl	CPL	CPL	WOA13/at rest
Years	1850–2013	1958–2013	1958–2013	1958–2013

Note. Modes: CPL = fully coupled, PCPL = partially coupled, OCO = ocean-only. The (spatial) forcing resolution indicates on which grid the momentum and freshwater fluxes are provided. Current feedback denotes whether the ocean current is considered for calculating the wind stress from 10 m wind.

ATLAS10-OCO was initialized in 1958 from rest, using temperature and salinity from the World Ocean Atlas 2013 (WOA13; Locarnini et al., 2013; Zweng et al., 2013) climatology and run for 56 years until 2013. A summary of all model experiments can be found in Table 1 and the years covered by the respective experiments are visualized in Figure 3a.

2.4. PCPL—Wind Stress and Buoyancy Forcing

Before studying the performance of partial coupling, we compare the wind stress and buoyancy forcing that is applied in the different model experiments.

The most important characteristics of the different wind stress forcings are visualized by timeseries of the zonal mean zonal wind stress at 47°N (Figure 3a). CPL and PCPL-H simulate a higher mean wind stress than OCO and PCPL-L. The magnitude and timing of variability is nearly the same in OCO, PCPL-L, and PCPL-H, but differs in CPL. In the following we analyze the wind stress in more detail focusing on the zonal mean zonal wind stress, due to its importance for the large-scale circulation (e.g., by setting the latitudinal position of basin scale oceanic gyres and impacting their strength based on Sverdrup theory).

The zonal mean zonal wind stress (Figure 3b) has nearly the same meridional structure in CPL and the two partially coupled experiments (PCPL-L and PCPL-H) when referring to the position of maxima and minima only. The PCPL-H and CPL climatologies are the same by construction. Note that small differences between PCPL-H and CPL are still possible, because they are only identical when averaged over the full forcing period (1958–2013), but here we solely consider the period used for further analysis in the following sections (1970–2013). The meridional structure in PCPL-L matches the (un-nested) FOCI-ensemble and is thus not tied to CPL's climatology. In CPL, due to the 2-way nesting, the higher resolution in the nest also affects the host, which in turn can change the atmospheric circulation compared to the FOCI-ensemble. However, this does not seem to notably alter the meridional structure of the zonal wind stress, as apparent in the very similar position of maxima and minima in PCPL-H/CPL and PCPL-L. It should be pointed out that neither monthly and annual anomalies, nor long-term trends in PCPL mode are affected by the replacement of the climatology, but are fully based on the reanalyzed wind stress.

In contrast, the mean strength differs between CPL/PCPL-H and PCPL-L, with the former having the strongest mean zonal wind stress at most latitudes. As a result, the wind stress curl in the center of the basin scale oceanic gyres is also stronger in CPL/PCPL-H (Figure 3c). While in PCPL-H a climatology based on the wind stress calculated by ECHAM6 during runtime is used, we employ the CORE bulk formula (Large & Yeager, 2009), that is also used in OCO, to derive the wind stress climatology from 10 m wind offline in PCPL-L. The online application of the ECHAM6 bulk formula (based on Louis (1979)) and the offline application of the CORE bulk formula results in a considerably different wind stress for the same 10 m wind. The result of these different strategies is one experiment being more comparable to CPL (PCPL-H) and the second being closer to OCO (PCPL-L). Both strategies have advantages and disadvantages. While the higher mean wind stress in PCPL-H is expected to

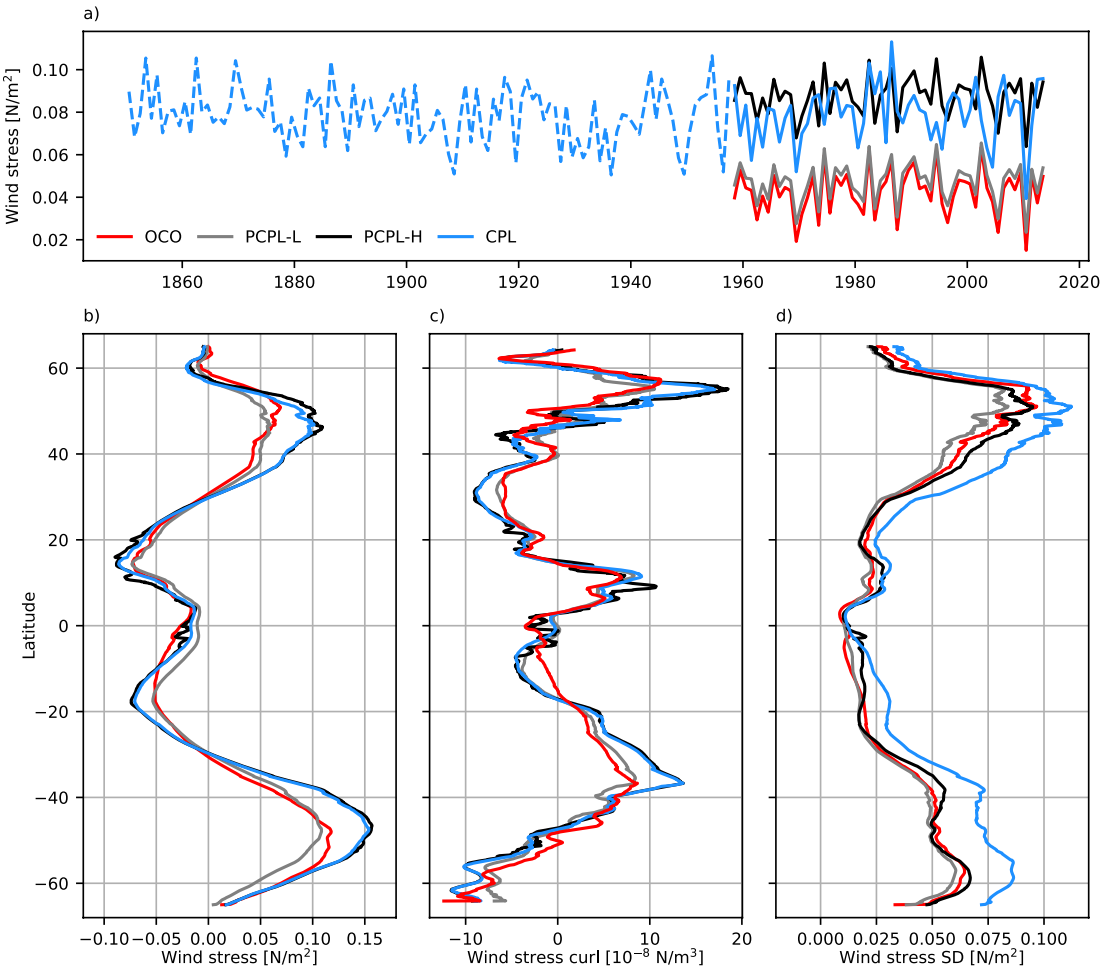

Figure 3. Timeseries of the annual mean zonal mean zonal wind stress at 47°N (a). The spin-up period of the fully coupled simulation is indicated by a dashed line. 1970–2013 zonal mean zonal wind stress (b), zonal mean wind stress curl (c) and standard deviation of the zonal mean zonal wind stress (d) in the Atlantic (including the Atlantic sector of the Southern Ocean).

minimize a secondary spin-up and subsequent model drift after switching to PCPL mode, the lower wind stress in PCPL-L allows for a better comparison to OCO. This is the comparison we are most interested in. By retaining the mean meridional structure of FOCI in PCPL-L, this spin-up may be less strong. In particular the position of the southern hemisphere westerlies differs considerably in FOCI and the reanalysis products.

Except for the equatorial region, CPL also shows the strongest zonal mean zonal wind stress variability (Figure 3d). This is likely caused by a combination of differences in the bulk formulae and the explicit simulation of feedbacks. Note that PCPL does exclude feedbacks that directly involve a surface momentum transfer. Further, the wind stress variability is very similar in PCPL-H and PCPL-L, since both are derived from reanalyzed 10 m wind using the offline CORE bulk formula. Neglecting ocean currents and atmospheric stability to create the PCPL forcing does not seem to have a large impact on the variability. In OCO wind stress is calculated during runtime incorporating the ocean and atmosphere's (provided by the forcing data set) states, but variability is comparable to the PCPL experiments (that use the same 10 m wind anomalies) at most latitudes. In particular there is not a bias toward lower, or higher, variability in both PCPL experiments. The meridional structure of wind stress variability is overall similar in the PCPL experiments and also compares well with OCO.

As visible in Figure 3a, wind stress variability at 47°N is highly correlated between PCPL-H, PCPL-L, and OCO by construction. This is true for all other latitudes as well. The fully coupled simulation is not correlated to OCO, nor the PCPL experiments.

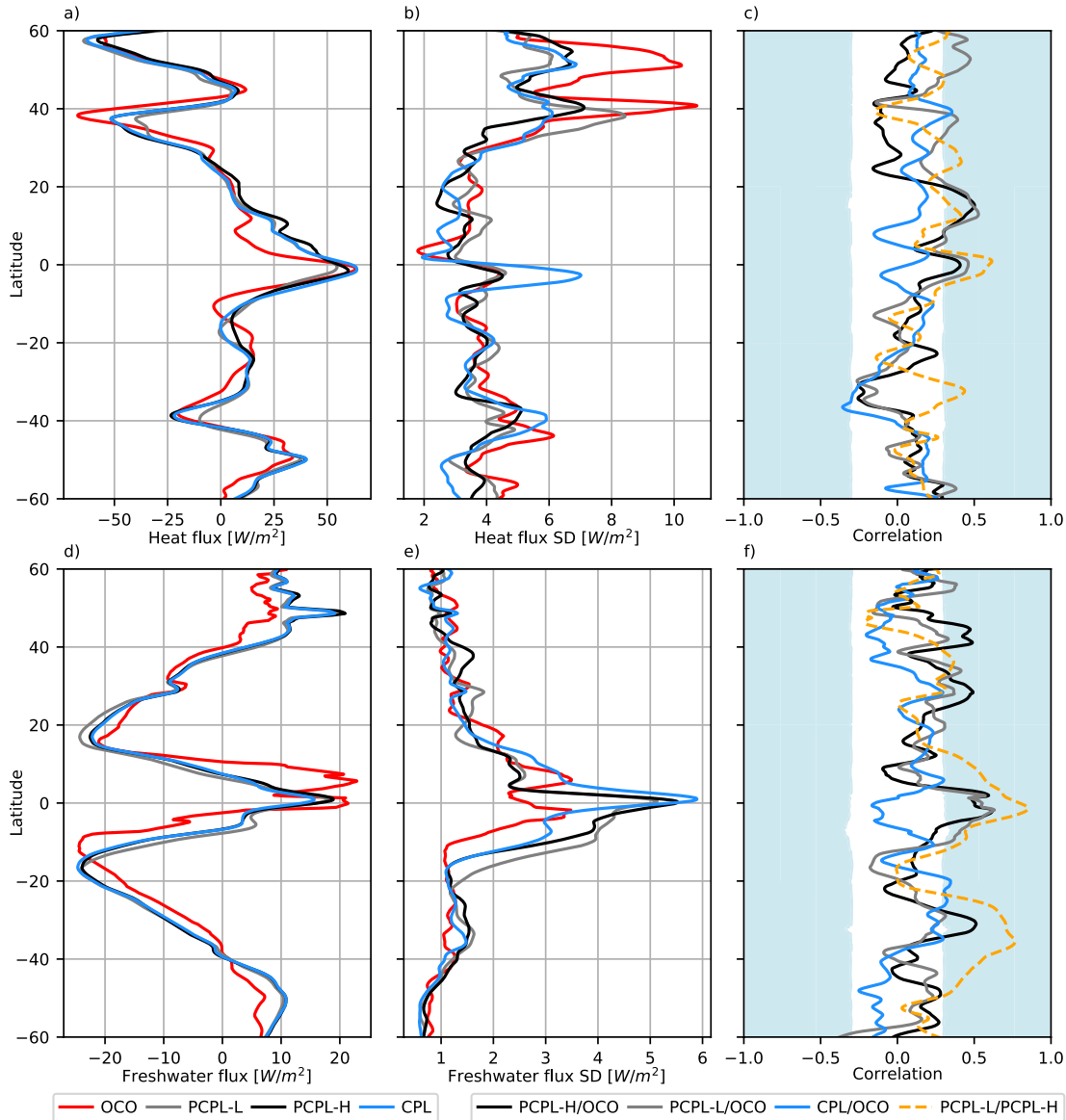

Figure 4. 1970–2013 zonal mean heat flux (a) and standard deviation (b) based on detrended annual means in the Atlantic (including the Atlantic sector of the Southern Ocean). Correlations of annual and zonal mean (detrended) heat fluxes are shown in (c). (d–f) analogously show the heat equivalent freshwater flux. Both fluxes are defined positive downward (ocean heat and freshwater gain). The fluxes were smoothed with a 31 grid point (3°) boxcar filter before calculating correlations.

As expected from the analysis by Thoma et al. (2015), partial coupling does not considerably change the mean heat and freshwater fluxes and their magnitude of variability (Figure 4). The freshwater flux is provided as a heat-equivalent freshwater flux here (e.g., Cerovečki et al., 2011). Both buoyancy flux components are very similar in PCPL-L/H and CPL. Differences to OCO are more pronounced, because of the very different approaches of calculating the surface boundary conditions in the coupled and un-coupled set-ups. Especially the stronger heat flux variability in the northern Atlantic and the increased tropical rainfall in OCO stand out. Overall, the assimilation of wind stress variability does not affect the timing of heat and freshwater flux variability in the Atlantic. The correlation is not significant, except for spikes at individual latitudes. Significance levels are calculated based on a two-sided student *t*-test, considering serial correlation by calculating effective degrees of freedom following Emery and Thomson (2001). Note that with a confidence interval of 95% there is still a 5% chance of falsely rejecting the null hypothesis (zero correlation). Such spikes likely have no physical meaning as long as they don't cover a larger latitude range, or are consistent across different experiments. The only region with a correlation that is significant for all experiments, except CPL/OCO, is the tropical Atlantic. It is possible that this

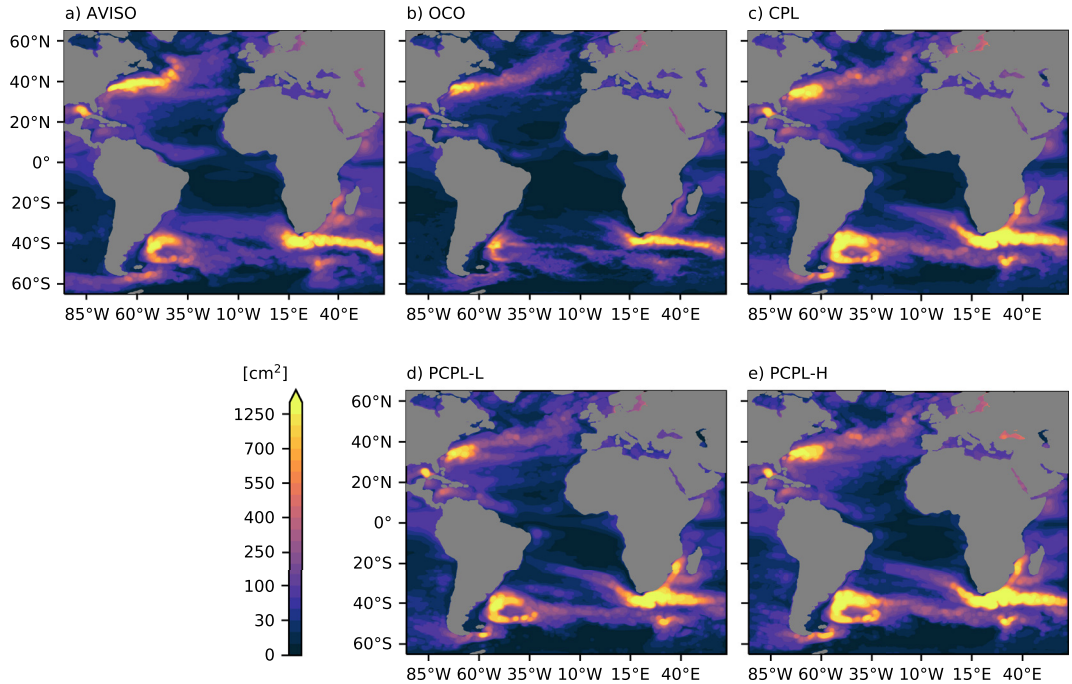

Figure 5. SSH variance (1993–2013) based on detrended 5-day means from AVISO (a), OCO (b), CPL (c) PCPL-L (d) and PCPL-H (e). All model fields show SSH variance on the nest grid.

correlation is caused by an atmospheric bridge to the equatorial Pacific and therefore mediated by the atmosphere models response to ENSO. Our PCPL experiments are very successful in reproducing the observed ENSO state, consistent with Thoma et al. (2015). As a result, also the timing of heat flux variability in the equatorial Pacific is significantly improved (Figure S1 in Supporting Information S1). The correlation of monthly Niño3.4 SST anomalies to observations (Rayner et al., 2003) is above 0.8 for both PCPL experiments and therefore even higher than reported by Thoma et al. (2015).

3. Mean State, Variability and Multidecadal Trends

In the following, we address our first question on the ability of the FOCI-ATLAS10 configuration and partial coupling to realistically reproduce the past large-scale circulation. We therefore analyze patterns of mesoscale activity and the vertically integrated (gyre) and zonally integrated (overturning) volume transports, the magnitude of their interannual variability and long term trends.

3.1. SSH Variance

A main benefit of a model at 1/10° resolution is the explicit simulation of mesoscale eddies in vast areas of the ocean. The surface circulation of the Atlantic is often dominated by mesoscale eddies, rather than coherent currents (e.g., Chelton et al., 2011). Their importance is also highlighted in studies showing a more realistic representation of the AMOC in high-resolution models (Hirschi et al., 2020). It is thus important to study, whether FOCI-ATLAS10 is able to adequately represent mesoscale activity and whether it changes in partial coupling mode.

At 1/10° resolution, ATLAS10 is able to simulate vigorous mesoscale activity throughout most of the Atlantic Ocean (Figure 5). Overall, the spatial patterns of SSH variability in CPL, OCO, PCPL-H, and PCPL-L are very similar and mostly agree with the SSH variance derived from satellite altimetry (AVISO). Especially in the Malvinas Confluence Zone and the Agulhas region. Also the western boundary north of the equator, including the Gulf of Mexico, and the NAC are characterized by strong eddy activity. It should be noted that the model simulates very few West Greenland Current eddies, compared to higher resolved models (Rieck et al., 2019). Also the north-west corner is not pronounced in ATLAS10 and high values of SSH variance along the NAC

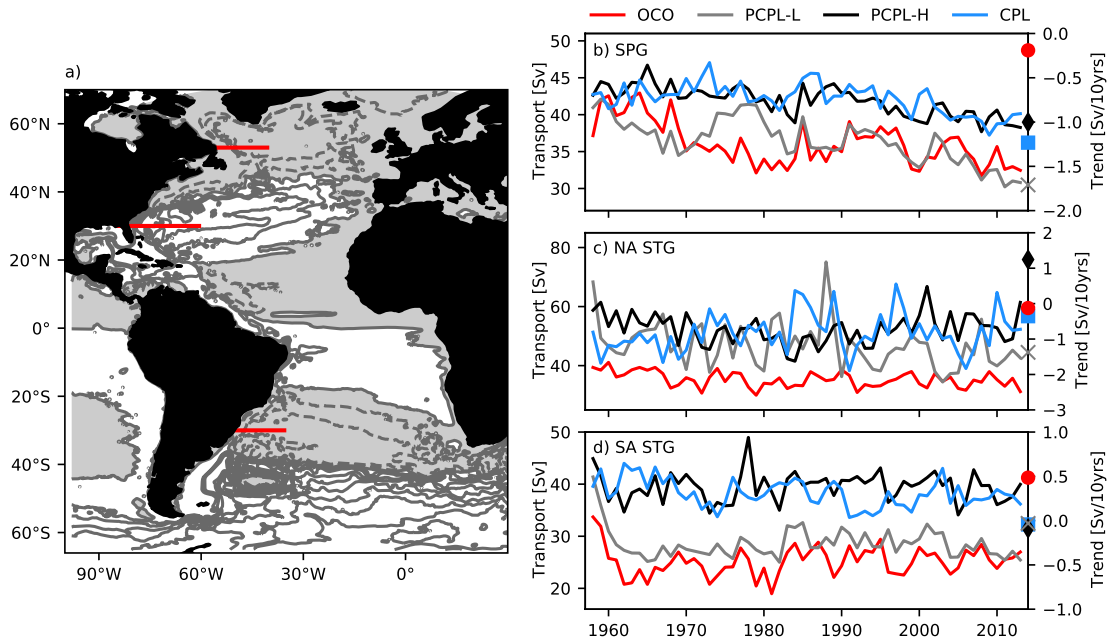

Figure 6. Horizontal gyre circulation: Mean (1970–2013) barotropic stream function in Sv from CPL (a). Annual mean transports of the Subpolar Gyre (b), North Atlantic Subtropical Gyre (c) and South Atlantic Subtropical Gyre (d). Linear trends (1970–2013) are marked on the right *y*-axis. The sections used to derive the gyre transports are shown in panel (a).

pathway are more confined to the North American coast, most likely as a consequence of the no-slip lateral boundary condition (Section 2.1). Another notable difference is seen in the pathway of Agulhas Rings. AVISO shows increased SSH variance between 40°S and 20°S extending across the full width of the Atlantic. SSH variance in OCO is clearly lower in this region, suggesting that Agulhas Rings are less intense, less frequent, or decay faster. In contrast, CPL shows a very strong and narrow pathway of Agulhas Rings that nearly reaches the western boundary. The partially coupled experiments show a very similar pathway. Based on sensitivity experiments with absolute and relative wind by Schwarzkopf et al. (2019), the interaction between the wind forcing and mesoscale Agulhas Rings is important for a realistic representation of the ring path. Even when using relative wind in FOCI-ATLAS10 (as in CPL), the wind stress calculation is performed on the coarser ECHAM6 grid and therefore the wind stress does not change across the eddy, excluding a feedback between the mesoscale current direction and the large scale wind. Also note the comparably high variance in the Caspian Sea in OCO. In contrast to all FOCI experiments (see Section 2), non-zero net freshwater fluxes in the Caspian Sea are allowed in OCO. Because of the prescribed atmosphere in OCO, unrealistic fluxes in the closed basin do not affect remote ocean areas.

Although the SSH variance is very heterogeneous, OCO shows the overall lowest variance, while PCPL-H and CPL simulate SSH variance that can be twice as large in certain regions (e.g., the Agulhas Retroflection). PCPL-L simulates variability with a magnitude in-between. This is true for SSH variance in the individual regions discussed above and also the full nest domain. The comparison between PCPL-H and PCPL-L suggests that the mean wind stress plays an important role for the magnitude of SSH variance.

3.2. Horizontal Gyre Circulation

General features of the long term mean gyre circulation (exemplarily shown for the fully coupled experiment (CPL) in Figure 6a) agree among all our simulations and are also in agreement with other models of comparable (or higher) resolution (e.g., Hirschi et al., 2020; Schwarzkopf et al., 2019). In the south Atlantic, the Drake Passage inflow turns northward into the highly variable region of the Malvinas confluence. Further north, the South Atlantic Subtropical Gyre (SA STG) covers the latitudes between 40°S and 20°S. In the North Atlantic positive stream function values, indicating the anticyclonic flow of the North Atlantic Subtropical Gyre (NA

STG), are seen between 18°N and 40°N. The Gulf Stream separates from the US coast just north of 34°N (Cape Hatteras). At higher latitudes CPL simulates a vigorous cyclonic flow associated with the Subpolar Gyre (SPG).

We define the gyre strength by evaluating the maximum (minimum) of the barotropic stream function for the NA STG (SPG and SA STG). We choose the latitudes of 53°N (SPG), 30°N (NA STG) and 30°S (SA STG). These sections are shown in Figure 6a.

The mean gyre circulation at all latitudes is similar in CPL and PCPL-H, both simulating a stronger transport compared to OCO and PCPL-L. This is consistent with the stronger mean wind stress curl and thus mainly caused by the different methodologies used to calculate the wind stress. For the SPG, where estimates from coupled models with comparable resolution are available, ATLAS10 simulates a similar mean gyre transport. The SPG transport ranges from 36 to 42 Sv in our set of model experiments, while Meccia et al. (2021) derive a range of 35–55 Sv. Their estimate for the NA STG transport (at 34°N) is 55–95 Sv; all experiments presented here, except OCO, simulate a mean transport within this range (58–76 Sv). OCO, the only ocean-only experiment, simulates a slightly weaker transport of 46 Sv. For further analysis we chose to not follow Meccia et al. (2021), because the estimated transport at 34°N is clearly affected by mesoscale recirculations and eddies. It is questionable, whether the barotropic stream function maximum at this latitude is a good estimate of the large-scale gyre strength. The effect can be reduced, but not eliminated, by instead calculating the gyre transport at 30°N, avoiding the highly eddying NAC. The NA STG transport is lower by 10–24 Sv when derived at 30°N. The mean transport of the SA STG ranges from 25 Sv in OCO and 29 Sv in PCPL-L to 38 Sv in CPL and 40 Sv in PCPL-H.

Interannual variability (standard deviation of detrended annual means) is comparable in all experiments, except for a lower variability of the NA STG in OCO. Note that models with the strongest mean transport not necessarily simulate the highest variability.

In all experiments, except OCO, the SPG transport shows a significant negative trend. Note that we calculate trends after 1970, to eliminate the initial spin-up phase of OCO and secondary spin-up after switching to PCPL mode in PCPL-L. The magnitude of the SPG trend is strongest in PCPL-L (−1.7 Sv/10 yrs) and lower, but still highly significant (p-value <0.01; the p-value denotes the probability of accepting the null-hypothesis, i.e., the trend is equal to 0) in PCPL-H (−1 Sv/10 yrs) and CPL (−1.2 Sv/10 yrs). Especially PCPL-H and CPL simulate a stable gyre transport until the late 1980s, before the transport starts to decline. Although slightly masked by a secondary spin-up, PCPL-L seems to simulate the onset of a long term negative trend in the same time period. The similar timing and magnitude of trends in PCPL-H and CPL suggest that they are related to the historic atmospheric boundary conditions that are applied in both experiments. The stronger trend in PCPL-L likely reflects a transient adjustment to the lower mean wind stress (curl) in the subpolar North Atlantic (SPNA) that adds to the weakening under rising CO_2 concentrations. Despite using the latitude of 30°N, the NA STG trends are clearly affected by the strong mesoscale activity and sensitive to the time period chosen. CPL and OCO do not simulate a significant trend. PCPL-L simulates a weakening, which is only significant for the time period 1958–2013 and again is most likely an adjustment to the lower mean wind stress (curl). PCPL-H shows a significant strengthening of 1.2 Sv/10 years for the time period 1970–2013 (p-value = 0.03). The multidecadal SA STG trends are not significantly different from zero in any experiment.

None of the mentioned (significant) trends are directly related to local changes in the wind field that are small in the North Atlantic. The wind stress curl trends at 53°N and 30°N are smaller than 0.22×10^{-8} N m^{-3}/10 years in CPL and smaller than 0.05×10^{-8} N m^{-3}/10 years in PCPL-L/H and OCO. All these trends are insignificant (p-value >0.58). It is more likely that they are related to the response of the oceanic circulation to the atmospheric boundary conditions in CPL and PCPL-H. PCPL-L shows a model drift toward a lower mean gyre strength over the full experiment. But this drift can be (mostly) eliminated by retaining the stronger mean wind stress of the fully coupled configuration. Therefore, we can state that PCPL in general is able to simulate a stable gyre circulation that is still free to adjust to changes in for example, the radiative forcing, as long as the coupled model's inherent wind stress climatology is used. This is an important result and may be useful to distinguish between artificial trends in ocean-only simulations and real trends that are forced by the surface boundary conditions. Note that the salinity restoring in an ocean-only experiments can locally counteract changes in the surface freshwater forcing, or ocean circulation, by restoring toward a climatological field.

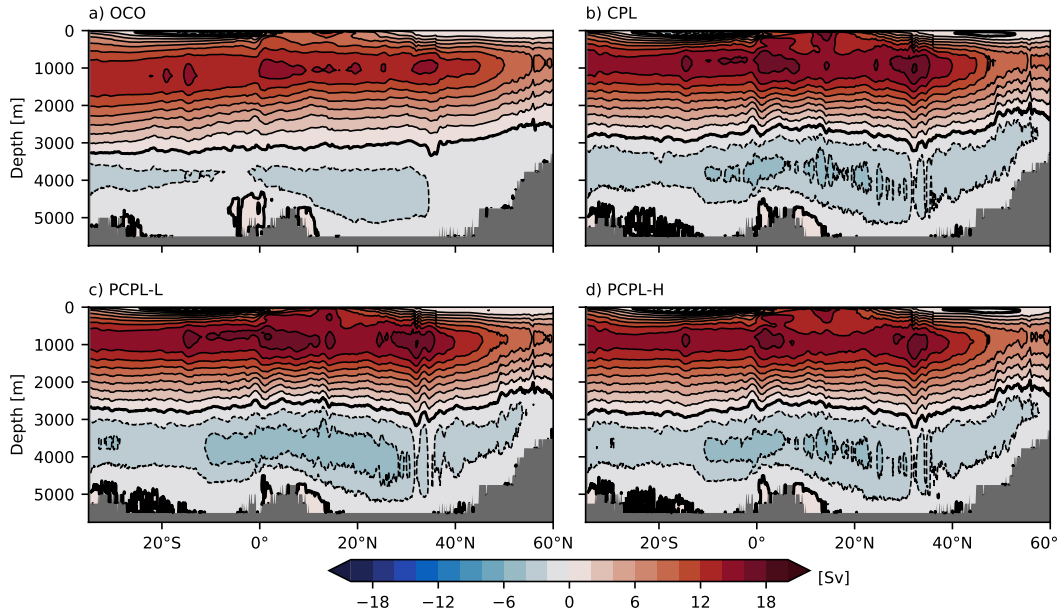

Figure 7. Mean 1970–2013 Meridional Overturning Stream function in OCO (a), CPL (b), PCPL-L (c) and PCPL-H (d). Contours are drawn with an interval of 2 Sv (the zero contour is drawn bold).

3.3. AMOC

The mean AMOC structure is similar in all model experiments, with a northward flow of surface water and a southward return flow of North Atlantic Deep Water (NADW) at mid-depth connected by sinking north of about 40°N (Figure 7). At abyssal depths the flow of Antarctic Bottom Water (AABW), formed in the Southern Ocean, is directed northward. Compared to OCO, the AABW and NADW cells, are clearly stronger in the (partially) coupled experiments, but the latter still covers a larger depth range in OCO. Especially south of 20°N, the zero-crossing of the Meridional Overturning Stream function is located approximately 500 m deeper in OCO. Since it continuously deepens toward the south in OCO, but slightly rises south of 20°S in PCPL and CPL, this difference can be as large as 700 m south of 20°S. This suggests that the shallower NADW cell in CPL, PCPL-L, and PCPL-H is not caused by reduced water mass transformation in the North Atlantic (NA), but a stronger formation of AABW. Although the mean wind stress in PCPL-H and PCPL-L considerably differs, the mean AMOC structure is still similar. PCPL-L simulates a slightly stronger NADW cell in the Subtropical Atlantic, and the AABW cell covers an even larger vertical range in the South Atlantic (SA) compared to CPL and PCPL-H. The NADW and AABW cells are nearly unchanged when PCPL-H is compared to CPL. The mean AMOC structure in density coordinates supports this result (Figure S2 in Supporting Information S1). Especially PCPL-H and CPL show little difference. In PCPL-L only the North Atlantic Shallow Tropical Cell is weaker, due to the lower mean wind stress. OCO simulates the weakest NADW cell in our set of experiments. The AMOC in density space (Figure S2 in Supporting Information S1) reveals that this is likely connected to reduced water mass transformation in the North Atlantic. Different mechanisms could be responsible for this result. In addition to different surface boundary conditions (including precipitation, runoff and heat fluxes), model choices such as SSS restoring and the advection scheme could be responsible. Also the initialization strategy differs. CPL (and therefore all FOCI-ATLAS10 experiments) is based on a 1,500-year long pre-industrial control simulation and therefore has a much longer spin-up time. OCO is initialized from climatological hydrography and an ocean at rest in 1958.

Figure 8 shows the temporal evolution of the AMOC strength at different latitudes of long-term measurements. The AMOC strength is defined as the maximum overturning stream function in depth or density space. In the SPNA the Overturning in the Subpolar North Atlantic Program (OSNAP) array measures the AMOC since 2014 and estimates a mean transport of 16.6 Sv (Lozier et al., 2019). Although the model experiments do not cover this time period, the AMOC transports in CPL (18.4 Sv), PCPL-H (17.6 Sv) and PCPL-L (17.3 Sv) are all slightly above the OSNAP estimate, while OCO simulates a weaker AMOC of 14.8 Sv. Overturning across the OSNAP section is calculated resembling observations and thus in density coordinates (here we use potential density

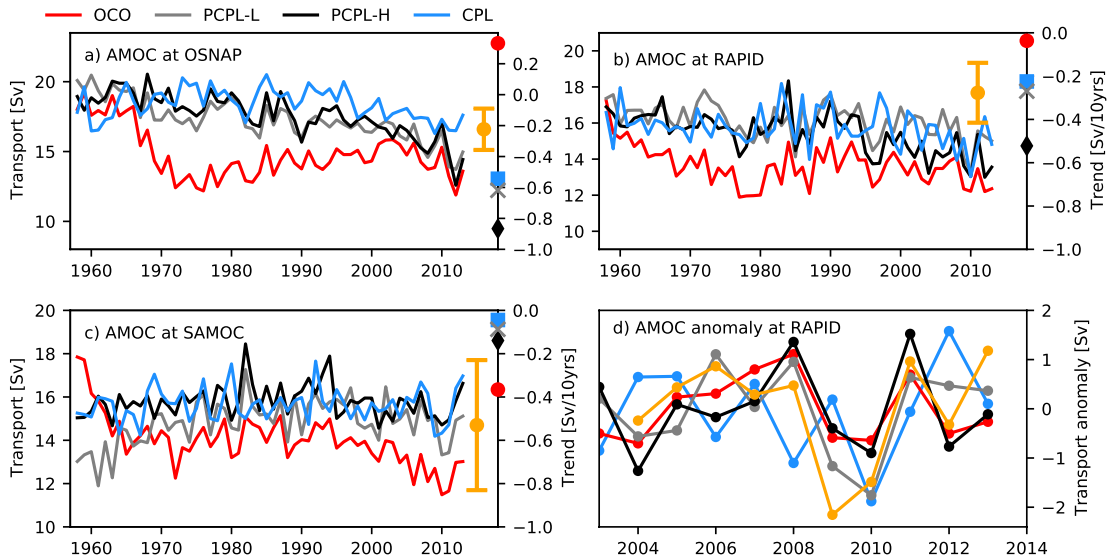

Figure 8. Annual mean Atlantic Meridional Overturning Circulation (AMOC) transports at the OSNAP (a), RAPID (26.5°N; b) and SAMOC (34.5°S; c) sections. Linear trends (1970–2013) are marked on the right *y*-axis. Observational mean and standard deviation from annual means are indicated by error bars in the center of the respective observational time period. Note that the observations do not cover the same time period shown for the model. Panel (d) shows the detrended AMOC anomaly at the RAPID section, including the observed timeseries (orange).

referenced to the surface). A similar result is obtained for the RAPID section at 26.5°N, where observations show a mean transport of 17.7 Sv (2004–2014; McCarthy et al., 2015). The model transports range from 15.8 to 16.1 Sv in the three FOCI-ATLAS10 experiments and 13.7 Sv in OCO. During the RAPID period (2004–2013), transports in the model are lower compared to the full timeseries and range between 13 Sv in OCO and 15.3 Sv in PCPL-L. In the South Atlantic (South Atlantic Meridional Overturning Circulation (SAMOC) section at 34.5°S) the difference between FOCI-ATLAS10 and the ocean-only configuration is less pronounced. Still OCO simulates the weakest AMOC strength (14.1 Sv). PCPL-L (14.8 Sv), PCPL-H (15.8 Sv) and CPL (15.6 Sv) all simulate a stronger overturning. All these estimates are close to the observed value (14.7 Sv; 2009–2018; Meinen et al., 2018). Both, RAPID and SAMOC, transports are calculated in depth space, for a better comparison to the observations, as the maximum of the overturning stream function below 500 m. As noted before, the mean AMOC is not highly sensitive to the mean wind stress forcing. PCPL-H and PCPL-L differ by less than 1 Sv despite the very different mean gyre transports.

In summary, the strength of the AMOC in the fully coupled and the two partially coupled simulations is similar, while it is slightly weaker in the ocean-only experiment. OCO shows a spin-up behavior until approximately 1970. While the AMOC strength is comparable to the PCPL experiments right after initialization at OSNAP and RAPID, it strongly decreases over the first years, before it stabilizes. As for the gyre transports, trends are calculated from 1970 to 2013 to exclude this initial spin-up phase. Still, there is a significant negative trend (p-value <0.01) at the OSNAP section in all experiments, except OCO. It is strongest in PCPL-H (−0.9 Sv/10 yrs) and weaker in PCPL-L (−0.6 Sv/10 yrs) and CPL (−0.5 Sv/10 yrs). OCO shows an increase of 0.4 Sv/10 years (p-value = 0.01).

AMOC trends at the RAPID section have the same sign as the OSNAP trends, but are weaker in PCPL-L, PCPL-H and CPL. The negative trend is again stronger in PCPL-H than in PCPL-L (−0.3 Sv/10 years, p-value = 0.02) and CPL (−0.2 Sv/10 years, not significant) and could reflect a downstream propagation of the signal seen at the OSNAP section. In this case it may be expected that the stronger trend in PCPL-H at OSNAP leads to a stronger trend at RAPID. Consistently, a weak positive OSNAP trend in OCO coincides with no trend at the RAPID section. It is somewhat surprising that, in contrast to the gyre transports, the trend is slightly stronger in PCPL-H than in PCPL-L. This suggest that the lower mean wind stress does not significantly reduce the NA overturning within 50 years. In general the magnitude of the NA AMOC change in the (partially) coupled experiments is comparable to estimates of the coupled CMIP6 ensemble (Weijer et al., 2020). The AMOC differences between the decades 2004–2013 and 1975–1984 at 26.5°N are −1.8 Sv (PCPL-H), −0.9 Sv (CPL) and −0.5 (PCPL-L).

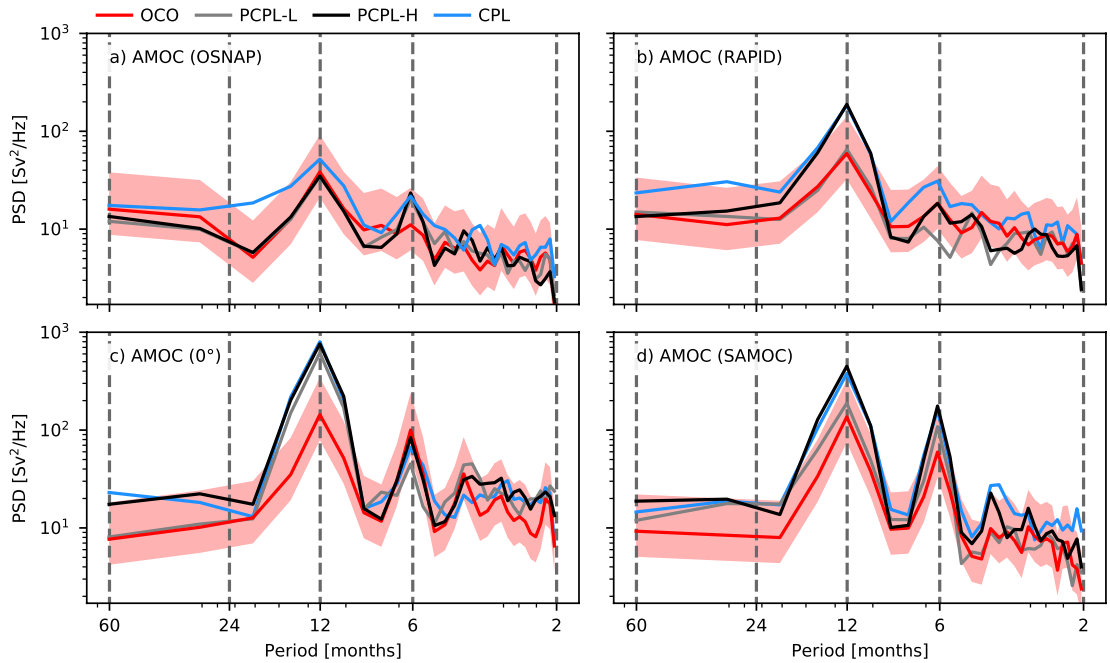

Figure 9. Power spectral density (PSD) of the Atlantic Meridional Overturning Circulation timeseries at OSNAP (a), RAPID (26.5°N; b), 0° (c) and SAMOC (34.5°S; d). Red shading shows the 95% confidence interval of the PSD estimate for OCO.

The CMIP6 ensemble shows a change between 0 and −4 Sv, with an ensemble mean of −1.2 Sv. This suggests that the trends in the (P)CPL experiments are a response to the atmospheric boundary conditions. To fully rule out that a model drift introduced by the partial coupling procedure exists, an additional set of experiments would be needed (e.g., a partially coupled experiment under pre-industrial atmospheric boundary conditions). However, based on the reasonable magnitude of the trends compared to the fully coupled experiment and other coupled models, we are confident that the AMOC in PCPL mode is not subject to significant model drift for the time period analyzed here. The different trends in OCO can be explained by various differences in the surface forcing compared to the (partially) coupled experiments, including the choices for the non-physical restoring term and the freshwater input provided by the forcing data set. Biastoch et al. (2021) showed that especially the AMOC trend is highly sensitive to small changes in the North Atlantic freshwater budget. They argue that a moderate negative AMOC trend after the 1990s is currently the best estimate, which would make the (P)CPL trends more realistic than the OCO trend.

At 34.5°S trends are close to zero and non-significant in PCPL-H/L and CPL. Only OCO still simulates a strongly negative trend with −0.4 Sv/10 years.

We investigate the variability of the AMOC in more detail by showing spectra of timeseries at 4 different latitudes (Figure 9). Additional to the already mentioned sections, we show the equatorial AMOC since it was shown to have distinct variability (Blaker et al., 2021). All following analysis is based on the period from 1970 to 2013 and the AMOC in z-coordinates, except for the overturning at OSNAP where density coordinates are used.

It is visible that the AMOC in CPL is most variable at all latitudes and on nearly all timescales. Still, on most timescales the difference between the experiments is not significant. In the North Atlantic, CPL simulates higher variability, especially at timescales longer than a year. At the equator both, CPL and PCPL-H simulate higher variability than OCO and PCPL-L, suggesting that the high variability could result from the higher mean wind stress. At the SAMOC section, only variability in CPL does not strongly decrease toward shorter timescales, causing the variability to be significantly higher than in all other experiments. The seasonal cycle at all latitudes is stronger in CPL than in OCO. Only at OSNAP it is also stronger than in PCPL-H, suggesting that it is not just determined by the magnitude of the wind stress' seasonal cycle (which is the same by construction due to the replaced climatology) in the SPNA. At the equator, the seasonal cycle is similarly strong in PCPL-H, PCPL-L and CPL. Here FOCI seems to exaggerate the seasonal cycle compared to the JRA55 reanalysis, independent of the

wind stress' seasonal cycle that is expected to be weaker in PCPL-L. At 34.5°S a pronounced semi-annual cycle exists in all simulations and also in observations (Meinen et al., 2018). A similar semi-annual cycle is present in all experiments at the equator. The strength of the semi-annual cycles is not systematically stronger/weaker in any of the configurations. While at SAMOC it is slightly more pronounced in (P)CPL than in OCO, the opposite is true at the equator. At OSNAP (P)CPL hints on a weak semi-annual cycle, but a similar peak is missing in OCO.

The overall higher variability of CPL compared to OCO could have different reasons. One is the stronger wind stress variability (likely dominant on short timescales) in CPL due to different strategies and formulae used to convert wind to wind stress. However, the difference on these timescale is very small except for mentioned difference at the SAMOC section. On timescales longer than a year the explicit simulation of feedbacks involving the wind forcing in CPL could cause higher variability. This seems to be important in the NA. PCPL excludes feedbacks that involve changes of the surface momentum transfer by prescribing the surface wind and shows lower variability with a magnitude comparable to OCO. In the SA this mechanisms seems to be less important, as variability in at least one PCPL experiment is similar to CPL.

Another interesting feature of the equatorial AMOC is a very strong increase of spectral power on timescales shorter than 1 month in agreement with Blaker et al. (2021). All experiments, including the partially coupled simulations, are able to simulate this high variability (not shown). This strong variability is also the reason to use the monthly mean AMOC here, since defining the AMOC strength based on 5-day means at the equator considerably changes the spectrum even on interannual timescales. A definition based on the monthly mean overturning stream function is more robust and representative for the strength of the NADW cell.

In conclusion, PCPL is able to retain the overall stable AMOC of the fully coupled simulation. Trends in the North Atlantic are similar in these experiments and possibly directly related to the applied historic atmospheric boundary conditions. This highlights the ability of PCPL to retain a stable AMOC, that is, maintain the important ocean-atmosphere feedbacks that were shown to be missing in forced experiments (e.g., Behrens et al., 2013), without the need to introduce an artificial modification of the surface water mass properties, or fluxes. Whether variability in PCPL mode is more similar to OCO or CPL depends on the latitude, timescale and mean wind stress of the PCPL forcing. In all cases differences are mostly non-significant. Thus, the magnitude of AMOC variability in PCPL mode is comparable to fully coupled and ocean-only experiments. In the next section we study, if PCPL is also able to reproduce the correct timing of this variability.

4. Timing of Variability

As exemplarily shown for FOCI-ATLAS10, coupled climate models are often able to simulate a realistic AMOC strength and magnitude of its variability. In order to study past AMOC changes, compare the model to observations and attribute extreme events to specific conditions, an ocean hindcast with the correct timing of variability is needed. This is generally not given in a coupled climate model and thus one of the main motivations to implement a partial coupling. Therefore, this section contains a detailed study of the timing of variability in the PCPL experiments.

First, we show the correlation between all experiments for the annual mean timeseries discussed before (time period 1970–2013). In order to study interannual variations, we remove low frequency variability from the timeseries by applying a 5-year highpass filter. This seems more reasonable than linear detrending, because linear detrending does not remove all low frequency variability.

Partial coupling does show skill to reproduce the timing of interannual variations of the SPG (Figure 10). The correlation between the SPG timeseries within the PCPL experiments (PCPL-L/PCPL-H) and between them and OCO is above 0.6 and significant based on a confidence level of 95%. Correlations for the NA STG are mostly insignificant, except for an anti-correlation between PCPL-L and OCO. The lack of correlation is probably a result of intrinsic, that is, unforced variability. The western branch of the NA STG gyre is characterized by strong mesoscale activity. Even different ocean-only simulations with the same forcing are not highly correlated in this region (not shown). The anti-correlation, although significant at 95%, is not expected to have a physical explanation. In contrast to the positive SPG correlations, it only occurs for one pair of experiments. For the SA STG we find a significant correlation of 0.4 between PCPL-H and OCO that could arise from the similar wind forcing. However, there is no correlation between PCPL-L and OCO, or PCPL-L and PCPL-H. The wind stress anomalies are derived from the same data set in all these experiments. This suggests that either the correlation

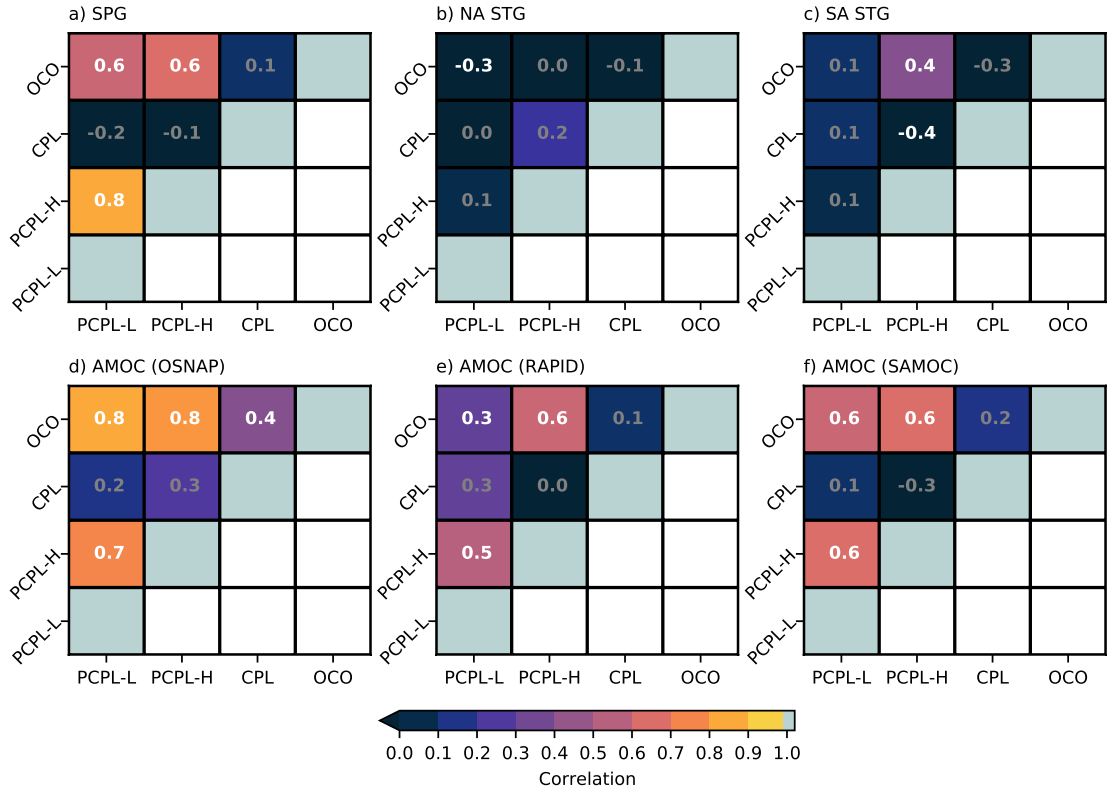

Figure 10. Correlation matrices for 5-year highpass filtered annual mean transport timeseries (1970–2013). (a) Subpolar Gyre, (b) North Atlantic Subtropical Gyre, (c) South Atlantic Subtropical Gyre, (d) Atlantic Meridional Overturning Circulation (AMOC) (OSNAP), (e) AMOC (RAPID; 26.5°N), (f) AMOC (SAMOC; 34.5°S). Correlations that are significant (not significant) based on a confidence level of 95% are displayed white (gray).

is significant by chance, or that the effect of wind variability is masked in PCPL-L. Note that mesoscale variability (SSH variance) is reduced in PCPL-L compared to PCPL-H, however, and probably not the cause here. A possible explanation is that the adjustment to the lower mean wind stress in PCPL-L has a non-linear impact on interannual variability (low frequency variability itself was removed by the filter before calculating the correlation). As expected, none of the gyre transports are significantly correlated between CPL and OCO. The high SPG correlation for both, PCPL-L and PCPL-H, but lack of robust STG correlation could be an expression of a stronger link between the gyre circulation and AMOC (discussed below). This is in line with Yeager (2020) reporting on a strong coupling of the density space AMOC and SPG transport variability.

For the AMOC, results are more robust across the different sections. Correlations between PCPL and OCO are significant and exceed 0.8 at OSNAP, 0.3 at RAPID and 0.6 at SAMOC. The correlations between PCPL-L and PCPL-H are similar to the correlations between PCPL (PCPL-H/PCPL-L) and OCO at the respective latitude. This gives confidence that the correlations are not just by chance, but indeed show an improved timing of variability in the PCPL experiments. Again CPL and OCO are uncorrelated, except for a positive correlation of 0.4 at the OSNAP section. CPL is not correlated to either PCPL experiment making it likely that this correlation is by chance.

An example for the ability of PCPL to simulate interannual variability of the AMOC is provided in Figure 8d. The strong minimum of the AMOC at 26.5°N in 2010 (McCarthy et al., 2012) is well reproduced in PCPL-L. The AMOC is rather stable until 2008, then drops by about 3 Sv and recovers to its previous strength by 2011 in PCPL-L and the RAPID observations. This result is in agreement with Thoma et al. (2015). PCPL-H and OCO simulate a similar temporal evolution, but underestimate the minimum. As a result, a secondary minimum in 2012 (which is also visible in observations) has nearly the same magnitude. The fully coupled (CPL) experiment does show a very different temporal evolution. Although the year 2010 shows a comparably weak AMOC transport, it does not stand out as clearly as in all other experiments and is most likely just co-incident.

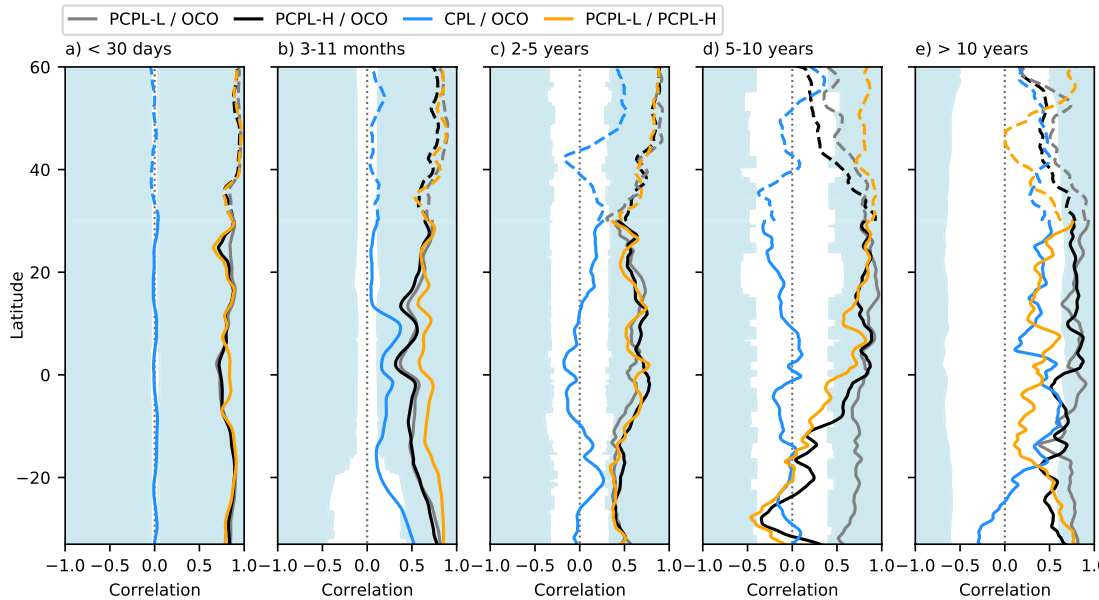

Figure 11. Correlation of the Atlantic Meridional Overturning Circulation (AMOC) transport in CPL / PCPL-L / PCPL-H, and OCO between 34°S and 60°N on different timescales. (a) high-frequency (30 days highpass filtered), (b) subannual (3–11 months bandpass filtered), (c) interannual (2–5 years bandpass filtered), (d) interannual—decadal (5–10 years bandpass filtered) and (e) decadal (10 years lowpass filtered and detrended) variability. Blue shading indicates correlation coefficients, that are statistically significant based on a confidence level of 95%. The meridional overturning stream function was smoothed with a 31 grid point (3°) boxcar filter before calculating the AMOC strength. South of 30°N the AMOC is calculated in depth space (solid), density coordinates are used further north (dashed). All timeseries start in 1970 and end half the filter time period prior to 2014.

So far we have only considered annual means, but the question remains whether PCPL is similarly successful in reproducing the timing of AMOC variability on shorter and longer timescales. Furthermore, the AMOC at specific latitudes may not be representative for the entire Atlantic and we expand our analysis to all latitudes between 34.5°S and 60°N. Here, the AMOC south of 30°N is defined as the maximum overturning stream function in depth space below 500 m. Since the subpolar North Atlantic overturning is more adequately represented in density coordinates (e.g., Lozier et al., 2019), we define the AMOC as the maximum overturning stream function in density space (potential density anomaly referenced to the surface) between 26.65 and 28 kg m^{-3} north of 30°N. All timeseries used for calculating correlations start in 1970 and end half the filtering time period prior to 2014.

It is clearly visible in Figure 11a that PCPL is capable of reproducing the correct timing of variability on short timescales (shorter than 1 month). The correlation between PCPL and OCO is around 0.8 at most latitudes. This very high correlation is likely a direct result of the wind-driven Ekman transport, shown to cause strong AMOC variability on short timescales (Cunningham et al., 2007). CPL, as expected, shows no significant correlation (95% confidence level). As mentioned before, significance levels are calculated based on a two-sided student *t*-test considering serial correlation by calculating effective degrees of freedom following Emery and Thomson (2001).

Note that we only define the AMOC strength using the 5-day mean overturning stream function to study the high frequency variability. For the following longer timescales we use monthly means, since they allow for a more robust estimate of the overturning strength close to the equator (see Section 3.3). Overall, the meridional structure of the correlation is similar for the subannual timescale (3–11 months; Figure 11b). The correlation between CPL and OCO is slightly higher, but mostly below 0.3. A considerable difference is an increase of the CPL/OCO correlation south of 20°S. As shown in Figure 9d, the AMOC shows a semi-annual cycle that is also visible in CPL. Therefore, not only the presence of this semi-annual cycle, but also its timing is reproduced in the fully coupled simulation to a certain extend. This suggests that the semi-annual cycle is a response to the atmospheric boundary conditions (e.g., solar radiation). Furthermore, a decrease in correlation to OCO between 30°N and 20°S with a minimum just north of the equator is visible for both, PCPL-L and PCPL-H. As the correlation between the two PCPL runs does not show this decrease, we suggest that differences in the representation of the equatorial circulation between the (partially-) coupled and un-coupled configurations could be the reason. The

corresponding currents span approximately the latitude range, where the correlation between PCPL and OCO differs most from the correlation between the two PCPL experiments.

On interannual timescales (2–5 years; Figure 11c), the correlation to OCO is significantly higher than zero at all latitudes in PCPL-L and PCPL-H. Thus, also on timescales longer than a year the assimilation of only wind stress anomalies can improve the timing of AMOC variability throughout the entire Atlantic. This result is in line with studies showing that the locally wind-driven Ekman transport also contributes to interannual variability (Blaker et al., 2015; McCarthy et al., 2012). Further, wind induced Ekman pumping and the resulting Sverdrup transport has an important impact on interannual AMOC variability (Duchez et al., 2014). The correlation decreases from values around 0.9 in the SPNA to 0.4 in the South Atlantic. This agrees with an increasing fraction of intrinsic interannual variability shown by Grégorio et al. (2015) and Leroux et al. (2018). In addition to this decrease toward the south, the correlation varies at individual sections. Just north of the southern tip of Africa there is local maximum in correlation that can explain the higher correlation at SAMOC than at RAPID seen before, especially for PCPL-L.

Even on interannual to decadal timescales (5–10 years; Figure 11d) the PCPL experiments show an improved timing of variability compared to CPL in the tropical and subtropical North Atlantic. PCPL-H and PCPL-L are both significantly correlated to OCO between the equator and 40°N. At subpolar latitudes the correlation between PCPL-H and OCO decreases to insignificant values north of 40°N. The PCPL-L/OCO correlation also decreases, but remains just at the margin of being significant, while the PCPL-L/PCPL-H correlation does not show a decrease. A possible explanation is an emerging impact of the upper ocean density, that was shown to be important for (multi-) decadal AMOC variability (Zhang et al., 2022). Although buoyancy fluxes are unconstrained in PCPL water mass properties are more similar between PCPL-H and PCPL-L than between the two experiments and OCO. This could lead to a similar AMOC response to the applied wind forcing in the two PCPL experiments. Differences between the experiments become visible south of the equator. While the PCPL-H/OCO correlation remains high to about 15°S and drops to insignificant values further south, the PCPL-L/OCO correlation remains high for the whole South Atlantic. At the same time the correlation between the two PCPL experiments strongly decreases and becomes negative south of 20°S. A possible explanation for the lower correlation at the southern boundary of the Atlantic is connected to the source of AMOC variability in the different experiments. While AMOC anomalies in the South Atlantic in PCPL-H seem to mostly enter the Atlantic from the south and spread toward the equator, such northward spreading anomalies are only visible in PCPL-L and OCO to about 25°S (not shown). North of this latitude anomalies spread predominantly southward in these experiments. The stronger and more northward penetrating anomalies generated in the Southern Ocean in PCPL-H, are likely connected to the strongly enhanced wind stress compared to OCO and PCPL-L. The stronger wind stress in PCPL-H drives more variable and deeper mixing in the Southern Ocean and could therefore enhance the production of bottom water that spreads northward into the Atlantic. Nevertheless, also PCPL-L shows enhanced Southern Ocean mixing compared to OCO, consistent with a slightly decreasing correlation south of 25°S.

On longer timescales (>10 years; Figure 11e), the two PCPL experiments are not correlated throughout most of the Atlantic. Still, both experiments are significantly correlated to OCO south of 40°N. Especially because the filtering period is long compared to the length of our timeseries and the magnitude of decadal variability is small in all experiments, the correlations between PCPL-H/L and OCO should be interpreted with caution here. Most studies identify the subpolar North Atlantic as the main source of decadal AMOC variability (e.g., Biastoch et al., 2008; Jackson et al., 2022; Megann et al., 2021; Robson et al., 2012). Although the buoyancy fluxes in PCPL mode are not constraint by observations, atmospheric teleconnections to the Pacific (where heat flux variability is fairly well reproduced in the equatorial region), or an accumulated effect of the improved timing of AMOC variability on interannual timescales, could also influence the North Atlantic buoyancy forcing. However, none of our analysis supports such a hypothesis. We have already shown in Section 2.4 that the timing of the annual mean buoyancy forcing in the Atlantic is not significantly changed by partial coupling. Acknowledging that fluxes in different seasons may have a different impact on AMOC variability, we repeat our analysis for the northern hemisphere winter (DJF) heat flux, but do not find major differences. The variability in winter is higher in CPL than in all other experiments, but the correlation is still insignificant between PCPL-L/H and OCO, not only on interannual, but also on decadal timescales (Figure S3 in Supporting Information S1). Furthermore, the zonal mean heat flux could not be representative for the heat flux in specific AMOC key regions. We also calculated correlations for the Labrador, Irminger and southern Nordic Seas heat fluxes. Especially buoyancy (mainly heat) fluxes in the first two regions were identified by Megann et al. (2021) to impact decadal AMOC variability.

Again, a significant correlation is not found between any of our experiments (except for PCPL-L and PCPL-H in the Nordic Seas on decadal timescales). Furthermore, the correlations only being significant south of 40°N makes the North Atlantic an even more unlikely source of the AMOC correlation between the PCPL experiments and OCO. Thus, assuming the correlations reflect a physical mechanism, the only possible explanation is an impact of low frequency variability of the wind stress itself via changes in the Ekman or Sverdrup transports. We do find decadal variability of the Sverdrup transport, derived from the JRA55-do forcing data set to match the AMOC evolution in PCPL-L/H and OCO at the RAPID and SAMOC sections (Figure S4 in Supporting Information S1). Note that decadal wind stress variability in all these experiment is the same by construction. There is a striking similarity between the Sverdrup and AMOC transports in PCPL-L and OCO (correlations exceed 0.7 at both sections). The correlation is similarly high in PCPL-H at the SAMOC section, but slightly lower and not significant at the RAPID section (0.5). Still there is a high agreement (and correlation) before the late 1990s. Note that a positive (negative) anomaly of the Sverdrup transport is associated with a stronger Sverdrup gyre in the northern (southern) hemisphere. Thus a spin-up of the gyre is associated with a spin-down of the AMOC in the northern hemisphere, which matches observations and other models (McCarthy et al., 2012; Yeager, 2015). In the southern hemisphere, however, the AMOC transport increases together with the Sverdrup gyre transport. We do find hints on anti-correlations (correlations) of the decadal gyre (estimated as described in Section 3.2) and AMOC transports in the northern (southern) hemisphere, but most of them are insignificant. It is likely that the aforementioned impact of mesoscale variability on our gyre estimate also masks the wind stress curl driven signals on longer timescale. The timeseries in Figure S4 in Supporting Information S1 further reveal, why in the mid-latitude North Atlantic the AMOC in PCPL-H and PCPL-L are significantly correlated to OCO, but not to each other. PCPL-L resembles the variability in OCO better than PCPL-H before the 2000s, while PCPL-H is more successful after 2000. Decadal Ekman transport anomalies are also significantly correlated with the AMOC transport, but their magnitude is negligible compared to the Sverdrup transport. Based on these results, we hypothesize that low frequency variability in mid-latitudes winds can force low frequency AMOC variability. In experiments with stronger buoyancy driven decadal variability in the SPNA, however, this is likely masked. It is interesting to note that a similar high correlation between the AMOC and Sverdrup transport can not be seen in CPL (not shown). It is beyond the scope of this study to make a conclusive statement on the impact of low frequency wind forcing on the AMOC, since a large set of longer sensitivity experiments would be required.

We conclude that a correct timing of AMOC variability in PCPL mode is robust on interannual and shorter timescales. On interannual-decadal timescales the correlation depends on the latitude and seems to be sensitive to the mean Southern Ocean wind stress in the SA and water mass properties in the NA. A model with smaller biases than FOCI[-ATLAS10] in those regions could be more successful in reproducing the timing of interannual-decadal variability. It is unlikely that partial coupling is able to reliably reproduce the timing of decadal AMOC variability. The timing of the buoyancy (heat and freshwater) flux variability is not in agreement with the ocean-only simulation. There could be an additional impact of low frequency wind driven variability on the AMOC that is reproduced in PCPL mode, but only apparent in the absence of strong buoyancy driven AMOC variability in the North Atlantic.

5. Summary and Conclusion

With this study we aim at improving ocean hindcast simulations by applying a technique known as partial coupling in an eddying coupled climate model, showing its capabilities and limitations and help to identify possible use cases. Furthermore, our study reveals important aspects of the impact of wind forcing on AMOC variability on different timescales. We motivated our research by asking the following questions:

Do PCPL experiments simulate a realistic mean large-scale circulation and multi-decadal trends?

The nested ATLAS10 configuration is able to simulate a realistic mean gyre circulation in the ocean-only, fully coupled and partially coupled set-ups. The mean gyre transports are mostly determined by the mean wind stress curl and thus depend on the exact procedure used to convert 10 m wind from reanalysis and the model to wind stress. Here we compare two partially coupled experiments, with different mean wind stress. While PCPL-L uses a mean wind stress similar to the ocean-only experiment, PCPL-H is designed to match the fully coupled configuration as close as possible. The disadvantage of the former is a short secondary spin-up phase when switching to PCPL mode and possible long term model drift. This is clearly visible in the gyre transports (especially the SPG transport), but the AMOC is less affected within 56 years after initialization. The higher mean wind stress

of PCPL-H minimizes an initialization shock, but is no longer comparable to the mean wind stress applied in the ocean-only reference experiment.

The magnitude of interannual transport variability is not systematically affected by partial coupling. Mesoscale activity, as an important part of the horizontal circulation, is also reasonably well represented at 1/10° resolution in many regions. CPL and both PCPL experiments simulate a too narrow Agulhas Ring path, which is a result of the coarse atmospheric resolution and additionally, the application of absolute wind in PCPL mode (compare Schwarzkopf et al., 2019).

The mean structure and strength of the AMOC is very similar in the CPL and PCPL experiments, but slightly weaker in the ocean-only configuration. Still, the NADW cell reaches deeper in OCO, probably caused by less formation of Antarctic Bottom Water. It is likely that substantial differences in the surface boundary conditions between forced and coupled set-ups have an important contribution to the weaker transport in OCO. It was shown that mean heat, freshwater and momentum fluxes differ compared to the (partially-) coupled FOCI-ATLAS10 experiments. Also differences outside the nest area, for example, in the Arctic Ocean, are likely to contribute (Biastoch et al., 2021). The mean AMOC strength is found to be weakly sensitive to the mean wind stress forcing and resulting mean gyre transports. The mean AMOC strength in PCPL-H and PCPL-L differs by less than 0.5 Sv in the SPNA and is also similar to the transport in CPL, despite SPG transports differing by several Sverdrups. In the subtropical Atlantic, between approximately 30°S and 30°N, the AMOC is stronger in PCPL-L, with differences below 1 Sv at most latitudes. At least in the northern hemisphere, this is consistent with the dynamic coupling of the NA STG and the AMOC. As described by Yeager (2015) and supported by Section 4, the NA STG and AMOC response to wind stress curl changes are of opposite sign. In PCPL-L the initial reduction in wind stress (curl) drives a decreasing NA STG transport and possibly results in a stronger mean AMOC compared to PCPL-H and CPL. At the SAMOC section the AMOC is about 1 Sv weaker in PCPL-L than in PCPL-H, possibly a direct response to the weaker southern hemisphere westerlies.

AMOC variability at the latitudes considered here is largest in CPL on most timescales, due to a higher wind stress (variability) and the explicit simulation of feedbacks that involve surface momentum fluxes. The latter seems to be more important in the North Atlantic. Dependent on latitude and timescale, PCPL-H is closer to OCO than to CPL, or vice versa. PCPL-L is more comparable to OCO on all timescales, except for the equatorial seasonal cycle. Because PCPL-H, PCPL-L and CPL all show nearly the same power at annual periods, the strong seasonal cycle is rather related to differences in the heat and freshwater flux variability in FOCI than to wind stress.

PCPL shows promising results to simulate reasonable long term trends, meaning trends are related to the applied surface forcing rather than model drift. Unrealistic large downward trends in the gyre transports, especially in the SPNA, are visible in PCPL-L, but can be eliminated by keeping the mean wind stress of the fully coupled configuration (depicted by PCPL-H). AMOC trends at OSNAP and RAPID are slightly stronger in PCPL-H than PCPL-L, but the RAPID trends in both experiments are comparable to trends in CPL and the CMIP6 ensemble (Weijer et al., 2020), suggesting that the historic atmospheric boundary conditions (e.g., rising greenhouse gas concentrations) are responsible for a weakened AMOC after the 1970s. As already argued above, the gyre and AMOC response to a reduction in wind stress curl is of opposite sign in the subtropics according to Yeager (2015). At least for the RAPID section, their results are consistent with a weaker declining trend in PCPL-L. Therefore, various local and remote processes contribute to the magnitude of the trend at the considered latitudes and we can not fully prove that partial coupling does not introduce a long term model drift. Still, our results strongly suggest that important ocean-atmosphere feedbacks are still maintained in PCPL mode. This is a success, since it shows that partial coupling allows to omit the SSS restoring necessary to obtain a stable AMOC in the ocean-only set-up.

Is the correct timing of (AMOC) variability in PCPL experiments limited to certain latitudes, or timescales?

In addition to a realistic mean circulation and long term evolution, an ocean hindcast should be characterized by the correct timing of variability on the timescale of interest. Thoma et al. (2015) already showed the success of partial coupling for interannual AMOC variability at 26.5°N. We were able to confirm this result in an eddying model configuration and to systematically study the limitations of partial coupling on various timescales and throughout the whole Atlantic Ocean, not only for the sake of model development, but also to gain insight into

the impact of wind forcing on AMOC variability. Our results are based on a comparison between the partially coupled and ocean-only experiments.

Overall, partial coupling is able to simulate the correct timing of AMOC variability on timescales from submonthly to interannual (periods shorter than approximately 5 years) independent of the procedure used to generate the anomaly forcing. The correlation between the PCPL experiments and OCO are mostly higher than 0.6 and significantly different from 0 at all latitudes. This result matches and confirms the current knowledge of processes contributing to AMOC variability on these timescales. Variability on short timescales was shown to be dominated by the wind-driven Ekman transport (Cunningham et al., 2007). Also on interannual timescales wind-forcing was shown to be the major driver for AMOC variability (Biastoch et al., 2008; Zhao & Johns, 2014). The latitudinal dependence, with higher correlations in the North Atlantic, is consistent with an increasing fraction of intrinsic variability (i.e., variability not related to the applied surface forcing) in the South Atlantic. Grégorio et al. (2015) derive a ratio of intrinsic to total interannual AMOC variance close to zero north of 45°N and up to 45% at 30°S. A similar dependency of intrinsic AMOC variability on the latitude was obtained by Leroux et al. (2018).

The strong impact of wind forcing does extend to interannual—decadal variability, but our results suggest that the upper ocean density becomes increasingly important in the subpolar North Atlantic. This hypothesis is based on results of Zhang et al. (2022) and the higher correlation between PCPL-H and PCPL-L compared to the correlation to OCO. As water mass properties in PCPL-H and PCPL-L are much more similar, the NA AMOC response to the same wind stress anomalies could be more similar as well. In the Southern Ocean the stronger mean wind stress in PCPL-H generates stronger AMOC anomalies, possibly connected to deep mixing events north of the ice edge. These anomalies penetrate further north into the SA than anomalies of Southern Ocean origin in PCPL-L and OCO at periods between 5 and 10 years. This causes the PCPL-H/OCO and PCPL-H/PCPL-L correlations to drop in the southern hemisphere on this timescale.

On timescales longer than 10 years the correlation between PCPL and OCO depends on the latitude. PCPL-L/H and OCO are significantly correlated south of 40°N. Most studies find buoyancy driven processes to dominate AMOC variability on decadal timescales (e.g., Biastoch et al., 2008; Jackson et al., 2022; Megann et al., 2021; Robson et al., 2012). Buoyancy fluxes are unconstrained in PCPL mode and there is no correlation between the PCPL and ocean-only experiments on interannual, or decadal, timescales. Therefore, it is unlikely that the mentioned AMOC correlation is caused by a feedback of interannual ocean variability driven by the wind stress on the low frequency buoyancy forcing. Instead, the correlation is more likely explained by an AMOC response to low frequency wind variability via changes in the Sverdrup transport. This is not necessarily in contradiction to the aforementioned studies highlighting the impact of buoyancy driven variability. All experiments, including OCO, simulate little decadal variability, suggesting that the impact of the SPNA heat flux variability is underestimated. In experiments with strong decadal variability of the SPNA overturning, we expect these processes to mask the wind contribution.

Our timeseries are not long enough to study variability on interdecadal timescales. Based on the results of Eden and Jung (2001), showing that the NA interdecadal (periods around 30 years) circulation variability is caused by the oceans response to NAO heat flux forcing, it is unlikely that PCPL is able to simulate the correct timing. Still, the AMV was shown to have an improved timing in PCPL simulations and an improved timing of multidecadal variability in the Pacific (PDO) may impact the Atlantic via teleconnections on longer timescales (Thoma et al., 2015).

Apart from the integrative quantity of the AMOC, other circulation metrics are less strongly correlated in PCPL and OCO. For the gyre estimates intrinsic (i.e., unforced) mesoscale variability of the eddying model seems to have a large impact. The same is true for individual currents, such as the Florida Strait transport, although we did not include the analysis here. Only the SPG is significantly correlated, which hints on a strong connection to the AMOC in agreement with Yeager (2020). Due to the computational cost of the eddying resolution, our experiments are limited to a single model run. Although our main conclusions are not expected to change, the spread of a partially coupled ensemble on different timescales could reveal more information about the robustness of the timing of AMOC variability in PCPL mode. At the same time, an ensemble at eddying resolution is often not feasible and thus the ability of a single run to reproduce the timing of variability studied here is highly relevant.

In summary, a main motivation to study partial coupling is the reduction of arbitrary choices in the surface boundary condition calculation of an ocean-only experiment. At the same time, the correct timing of ocean

circulation variability in such forced simulations should be retained as good as possible, which is not given in fully coupled experiments. Our results show that PCPL can achieve the first goal. Both PCPL experiments simulate a stable AMOC with trends comparable to the fully coupled experiment. Further, the magnitude and timing of AMOC variability on timescales shorter than 5 years is well reproduced. Although we find an AMOC correlation between PCPL and OCO outside subpolar latitudes caused by low frequency wind variability, we do not find any hints that partial coupling does impact the timing of buoyancy flux variability in the North Atlantic. As a result, a single PCPL experiment can not be expected to reproduce the timing of decadal AMOC variability, limiting its applicability for the use case of hindcast simulations. However, the correct timing of AMOC variability on short and interannual timescales, together with a stable AMOC over multiple decades, can be useful for all studies focusing on sub-decadal processes. Note that the (partially) coupled configuration is only marginally more computational expensive than the ocean-only configuration, if run with a coarse atmospheric resolution. For a new configuration that is to be used to study interannual AMOC variability, it can be advantageous to use a partially coupled model. It avoids several arbitrary choices, not only restoring and budget corrections, but also details of the runoff interpolation that is typically not provided on the model grid.

There are many more use cases in sensitivity experiments that focus on specific processes, rather than reproducing past ocean variability in general. As presented here, PCPL is useful to assess the impact of wind forcing on the AMOC. In addition, PCPL allows to infer the ocean's dynamical role in driving atmospheric variability. As an example, the 2009/2010 minimum of the AMOC is expected to have changed the ocean heat transport (McCarthy et al., 2012) and could have fed back to the atmosphere. PCPL allows to study, whether the AMOC downturn did change the atmospheric circulation and contributed to the strongly negative winter NAO phase in the winters of 2009/2010 and 2010/2011 (Buchan et al., 2014). This would not be possible in a fully coupled configuration, since it is not expected to reproduce the same AMOC minimum. Neither it could be studied in an ocean-only set-up, because the atmospheric state is prescribed. An application of PCPL in ocean modeling could focus on linkages between the AMOC and SPG transports, since the timing of both is very well reproduced in PCPL. By prescribing different wind patterns in a coupled model it is possible to investigate the nature of this linkage, without altering the response by also prescribing heat and freshwater fluxes. Furthermore, the good performance of PCPL in the tropical Pacific and hints on an improved timing of buoyancy flux variability in the tropical Atlantic could be interesting for studies on teleconnections between the two ocean basins in tropical latitudes.

The capabilities identified here make partial coupling an interesting addition to ocean-only and coupled models as discussed above. At the same time, it was not possible to make conclusive statements about the timing of decadal variability in partially coupled models that would be needed for the application in hindcast simulations. This may provide further motivation to expand our analysis and investigate modifications to the partial coupling procedure in order to perform successful ocean hindcasts in earth system models.

Data Availability Statement

All data shown in the figures, scripts, model name lists and essential model input is publicly available (Schulzki et al., 2022) at: https://hdl.handle.net/20.500.12085/57ea9d04-2bd4-4a27-8994-3e19982731bd. The Ssalto/Duacs altimeter products (Taburet & Pujol, 2022) were produced and distributed by the Copernicus Marine and Environment Monitoring Service (CMEMS), https://marine.copernicus.eu/. OSNAP data (Li et al., 2021) were collected and made freely available by the OSNAP (Overturning in the Subpolar North Atlantic Program) project and all the national programs that contribute to it (www.o-snap.org). Data from the RAPID AMOC monitoring project (Frajka-Williams et al., 2021) is funded by the Natural Environment Research Council and are freely available from www.rapid.ac.uk/rapidmoc.

Acknowledgments
The authors gratefully acknowledge the Earth System Modelling Project (ESM) for funding this work by providing computing time on the ESM partition of the supercomputer JUWELS (Jülich Supercomputing Centre, 2019) at the Jülich Supercomputing Centre (JSC). The study was supported by the European Union's Horizon 2020 research and innovation programme under grant agreement No. 818123 (iAtlantic). We thank 3 anonymous reviewers for their many constructive comments and helpful suggestions during the review process which helped to improve our manuscript.

References

Amante, C., & Eakins, B. (2009). ETOPO1 1 arc-minute global relief model: Procedures. *NOAA Technical Memorandum NESDIS. NGDC-24*. https://doi.org/10.7289/V5C8276M

Arakawa, A., & Hsu, Y.-J. G. (1990). Energy conserving and potential-enstrophy dissipating schemes for the shallow water equations. *Monthly Weather Review*, *118*(10), 1960–1969. https://doi.org/10.1175/1520-0493(1990)118⟨1960:ECAPED⟩2.0.CO;2

Barnier, B., Madec, G., Penduff, T., Molines, J.-M., Treguier, A.-M., Le Sommer, J., et al. (2006). Impact of partial steps and momentum advection schemes in a global ocean circulation model at eddy-permitting resolution. *Ocean Dynamics*, *56*(5), 543–567. https://doi.org/10.1007/s10236-006-0082-1

Behrens, E., Biastoch, A., & Böning, C. W. (2013). Spurious AMOC trends in global ocean sea-ice models related to subarctic freshwater forcing. *Ocean Modelling*, *69*, 39–49. https://doi.org/10.1016/j.ocemod.2013.05.004

Biastoch, A., Böning, C. W., Getzlaff, J., Molines, J.-M., & Madec, G. (2008). Causes of interannual–decadal variability in the meridional overturning circulation of the midlatitude North Atlantic Ocean. *Journal of Climate*, *21*(24), 6599–6615. https://doi.org/10.1175/2008JCLI2404.1

Biastoch, A., Schwarzkopf, F. U., Getzlaff, K., Rühs, S., Martin, T., Scheinert, M., et al. (2021). Regional imprints of changes in the Atlantic Meridional Overturning Circulation in the eddy-rich ocean model VIKING20X. *Ocean Science*, *17*(5), 1177–1211. https://doi.org/10.5194/os-17-1177-2021

Blaker, A. T., Hirschi, J. J.-M., Bell, M. J., & Bokota, A. (2021). Wind-driven oscillations in the meridional overturning circulation near the equator. Part I: Numerical models. *Journal of Physical Oceanography*, *51*(3), 645–661. https://doi.org/10.1175/JPO-D-19-0296.1

Blaker, A. T., Hirschi, J. J.-M., McCarthy, G., Sinha, B., Taws, S., Marsh, R., et al. (2015). Historical analogues of the recent extreme minima observed in the Atlantic Meridional Overturning Circulation at 26°N. *Climate Dynamics*, *44*(1), 457–473. https://doi.org/10.1007/s00382-014-2274-6

Blanke, B., & Delecluse, P. (1993). Variability of the tropical Atlantic Ocean simulated by a general circulation model with two different mixed-layer physics. *Journal of Physical Oceanography*, *23*(7), 1363–1388. https://doi.org/10.1175/1520-0485(1993)023⟨1363:VOTTAO⟩2.0.CO;2

Bougeault, P., & Lacarrere, P. (1989). Parameterization of Orography-induced turbulence in a Mesobeta–scale model. *Monthly Weather Review*, *117*(8), 1872–1890. https://doi.org/10.1175/1520-0493(1989)117⟨1872:POOITI⟩2.0.CO;2

Brovkin, V., Raddatz, T., Reick, C. H., Claussen, M., & Gayler, V. (2009). Global biogeophysical interactions between forest and climate. *Geophysical Research Letters*, *36*(7). https://doi.org/10.1029/2009GL037543

Buchan, J., Hirschi, J. J.-M., Blaker, A. T., & Sinha, B. (2014). North Atlantic SST anomalies and the Cold North European weather events of winter 2009/10 and December 2010. *Monthly Weather Review*, *142*(2), 922–932. https://doi.org/10.1175/MWR-D-13-00104.1

Cerovečki, I., Talley, L. D., & Mazloff, M. R. (2011). A comparison of Southern Ocean air–sea buoyancy flux from an ocean state estimate with five other products. *Journal of Climate*, *24*(24), 6283–6306. https://doi.org/10.1175/2011JCLI3858.1

Chelton, D. B., Schlax, M. G., & Samelson, R. M. (2011). Global observations of nonlinear mesoscale eddies. *Progress in Oceanography*, *91*(2), 167–216. https://doi.org/10.1016/j.pocean.2011.01.002

Cheng, W., Chiang, J. C. H., & Zhang, D. (2013). Atlantic Meridional Overturning Circulation (AMOC) in CMIP5 models: RCP and historical simulations. *Journal of Climate*, *26*(18), 7187–7197. https://doi.org/10.1175/JCLI-D-12-00496.1

Cunningham, S. A., Kanzow, T., Rayner, D., Baringer, M. O., Johns, W. E., Marotzke, J., et al. (2007). Temporal variability of the Atlantic Meridional Overturning Circulation at 26.5°N. *Science*, *317*(5840), 935–938. https://doi.org/10.1126/science.1141304

Danabasoglu, G., Yeager, S. G., Bailey, D., Behrens, E., Bentsen, M., Bi, D., et al. (2014). North Atlantic simulations in coordinated ocean-ice reference experiments phase II (CORE-II). Part I: Mean states. *Ocean Modelling*, *73*, 76–107. https://doi.org/10.1016/j.ocemod.2013.10.005

Debreu, L., Vouland, C., & Blayo, E. (2008). AGRIF: Adaptive grid refinement in Fortran. *Computers & Geosciences*, *34*(1), 8–13. https://doi.org/10.1016/j.cageo.2007.01.009

Ding, H., Greatbatch, R. J., Latif, M., Park, W., & Gerdes, R. (2013). Hindcast of the 1976/77 and 1998/99 climate shifts in the Pacific. *Journal of Climate*, *26*(19), 7650–7661. https://doi.org/10.1175/JCLI-D-12-00626.1

Duchez, A., Hirschi, J. J.-M., Cunningham, S. A., Blaker, A. T., Bryden, H. L., de Cuevas, B., et al. (2014). A new index for the Atlantic Meridional Overturning Circulation at 26°N. *Journal of Climate*, *27*(17), 6439–6455. https://doi.org/10.1175/JCLI-D-13-00052.1

Eden, C., & Jung, T. (2001). North Atlantic interdecadal variability: Oceanic response to the North Atlantic Oscillation (1865–1997). *Journal of Climate*, *14*(5), 676–691. https://doi.org/10.1175/1520-0442(2001)014⟨0676:NAIVOR⟩2.0.CO;2

Emery, W. J., & Thomson, R. E. (2001). Chapter 5—Time-series analysis methods. In W. J. Emery & R. E. Thomson (Eds.), *Data analysis methods in physical oceanography* (pp. 371–567). Elsevier Science. https://doi.org/10.1016/B978-044450756-3/50006-X

Farrow, D. E., & Stevens, D. P. (1995). A new tracer advection scheme for bryan and Cox type ocean general circulation models. *Journal of Physical Oceanography*, *25*(7), 1731–1741. https://doi.org/10.1175/1520-0485(1995)025⟨1731:ANTASF⟩2.0.CO;2

Fichefet, T., & Maqueda, M. A. M. (1997). Sensitivity of a global sea ice model to the treatment of ice thermodynamics and dynamics. *Journal of Geophysical Research*, *102*(C6), 12609–12646. https://doi.org/10.1029/97JC00480

Flato, G., Marotzke, J., Abiodun, B., Braconnot, P., Chou, S. C., Collins, W., et al. (Eds.). Climate change 2013: The physical science basis. Contribution of working group I to the fifth assessment report of the intergovernmental panel on climate change (pp. 741–882). Cambridge University Press. https://doi.org/10.1017/CBO9781107415324.020

Frajka-Williams, E., Moat, B., Smeed, D., Rayner, D., Johns, W., Baringer, M., et al. (2021). Atlantic Meridional Overturning Circulation observed by the RAPID-MOCHA-WBTS (RAPID-Meridional overturning circulation and heatflux array-western boundary time series) array at 26N from 2004 to 2020 (v2020.1) [Dataset]. NERC EDS British Oceanographic Data Centre NOC. https://doi.org/10.5285/cc1e34b3-3385-662b-e053-6c86abc03444

Gent, P. R., & Mcwilliams, J. C. (1990). Isopycnal mixing in ocean circulation models. *Journal of Physical Oceanography*, *20*(1), 150–155. https://doi.org/10.1175/1520-0485(1990)020⟨0150:IMIOCM⟩2.0.CO;2

Grégorio, S., Penduff, T., Sérazin, G., Molines, J.-M., Barnier, B., & Hirschi, J. (2015). Intrinsic variability of the Atlantic Meridional Overturning Circulation at interannual-to-multidecadal time scales. *Journal of Physical Oceanography*, *45*(7), 1929–1946. https://doi.org/10.1175/JPO-D-14-0163.1

Griffies, S. M., Biastoch, A., Böning, C., Bryan, F., Danabasoglu, G., Chassignet, E. P., et al. (2009). Coordinated Ocean-Ice reference experiments (COREs). *Ocean Modelling*, *26*(1), 1–46. https://doi.org/10.1016/j.ocemod.2008.08.007

Hallberg, R., & Gnanadesikan, A. (2006). The role of eddies in determining the structure and response of the wind-driven southern hemisphere overturning: Results from the modeling eddies in the Southern Ocean (MESO) project. *Journal of Physical Oceanography*, *36*(12), 2232–2252. https://doi.org/10.1175/JPO2980.1

Hirschi, J. J.-M., Barnier, B., Böning, C., Biastoch, A., Blaker, A. T., Coward, A., et al. (2020). The Atlantic Meridional Overturning Circulation in high-resolution models. *Journal of Geophysical Research: Oceans*, *125*(4), e2019JC015522. https://doi.org/10.1029/2019JC015522

Jackson, L. C., Biastoch, A., Buckley, M. W., Desbruyères, D. G., Frajka-Williams, E., Moat, B., & Robson, J. (2022). The evolution of the North Atlantic Meridional Overturning Circulation since 1980. *Nature Reviews Earth & Environment*, *3*(4), 241–254. https://doi.org/10.1038/s43017-022-00263-2

Jülich Supercomputing Centre. (2019). JUWELS: Modular tier-0/1 supercomputer at the Jülich supercomputing centre. *Journal of Large-Scale Research Facilities*, *5*(A135). https://doi.org/10.17815/jlsrf-5-171

Large, W. G., & Yeager, S. G. (2009). The global climatology of an interannually varying air–sea flux data set. *Climate Dynamics*, *33*(2), 341–364. https://doi.org/10.1007/s00382-008-0441-3

Lemarié, F. (2006). NEMO/AGRIF nesting tools, User's Guide (30 January 2006). Retrieved from https://forge.ipsl.jussieu.fr/nemo/wiki/Users/SetupNewConfiguration/AGRIF-nesting-tool

Leroux, S., Penduff, T., Bessières, L., Molines, J.-M., Brankart, J.-M., Sérazin, G., et al. (2018). Intrinsic and atmospherically forced variability of the AMOC: Insights from a large-ensemble ocean hindcast. *Journal of Climate*, *31*(3), 1183–1203. https://doi.org/10.1175/JCLI-D-17-0168.1

Li, F., Lozier, M. S., Bacon, S., Bower, A., Cunningham, S., de Jong, M., et al. (2021). Meridional overturning circulation observed by the OSNAP (overturning in the Subpolar North Atlantic program) array from August 2014 to May 2018 [Dataset]. Georgia Institute of Technology. https://doi.org/10.35090/gatech/65537

Locarnini, R. A., Mishonov, A. V., Antonov, J. I., Boyer, T. P., Garcia, H. E., Baranova, O. K., et al. (2013). World Ocean Atlas 2013, volume 1: Temperature (Technical Report No. NOAA Atlas NESDIS 73).

Louis, J.-F. (1979). A parametric model of vertical eddy fluxes in the atmosphere. *Boundary-Layer Meteorology*, *17*(2), 187–202. https://doi.org/10.1007/BF00117978

Lozier, M. S. (2012). Overturning in the North Atlantic. *Annual Review of Marine Science*, *4*(1), 291–315. https://doi.org/10.1146/annurev-marine-120710-100740

Lozier, M. S., Li, F., Bacon, S., Bahr, F., Bower, A. S., Cunningham, S. A., et al. (2019). A sea change in our view of overturning in the subpolar North Atlantic. *Science*, *363*(6426), 516–521. https://doi.org/10.1126/science.aau6592

Madec, G. (2016). *NEMO ocean engine*. Note du Pole de modelisation, Institut Pierre-Simon Laplace (IPSL), France. No 27, ISSN No 1288-1619.

Martin, T. (2021). Runoff remapping for ocean model forcing. https://doi.org/10.3289/SW_2_2021

Matthes, K., Biastoch, A., Wahl, S., Harlaß, J., Martin, T., Brücher, T., et al. (2020). The flexible ocean and climate infrastructure version 1 (FOCI1): Mean state and variability. *Geoscientific Model Development Discussions*, *2020*, 1–53. https://doi.org/10.5194/gmd-2019-306

McCarthy, G., Frajka-Williams, E., Johns, W. E., Baringer, M. O., Meinen, C. S., Bryden, H. L., et al. (2012). Observed interannual variability of the Atlantic Meridional Overturning Circulation at 26.5°N. *Geophysical Research Letters*, *39*(19). https://doi.org/10.1029/2012GL052933

McCarthy, G., Smeed, D., Johns, W., Frajka-Williams, E., Moat, B., Rayner, D., et al. (2015). Measuring the Atlantic Meridional Overturning Circulation at 26°N. *Progress in Oceanography*, *130*, 91–111. https://doi.org/10.1016/j.pocean.2014.10.006

Meccia, V. L., Iovino, D., & Bellucci, A. (2021). North Atlantic gyre circulation in PRIMAVERA models. *Climate Dynamics*, *56*(11), 4075–4090. https://doi.org/10.1007/s00382-021-05686-z

Megann, A., Blaker, A., Josey, S., New, A., & Sinha, B. (2021). Mechanisms for late 20th and early 21st century decadal AMOC variability. *Journal of Geophysical Research: Oceans*, *126*(12), e2021JC017865. https://doi.org/10.1029/2021JC017865

Meinen, C. S., Speich, S., Piola, A. R., Ansorge, I., Campos, E., Kersalé, M., et al. (2018). Meridional overturning circulation transport variability at 34.5°S during 2009–2017: Baroclinic and barotropic flows and the dueling influence of the boundaries. *Geophysical Research Letters*, *45*(9), 4180–4188. https://doi.org/10.1029/2018GL077408

Meinshausen, M., Vogel, E., Nauels, A., Lorbacher, K., Meinshausen, N., Etheridge, D. M., et al. (2017). Historical greenhouse gas concentrations for climate modelling (CMIP6). *Geoscientific Model Development*, *10*(5), 2057–2116. https://doi.org/10.5194/gmd-10-2057-2017

Müller, W. A., Jungclaus, J. H., Mauritsen, T., Baehr, J., Bittner, M., Budich, R., et al. (2018). A higher-resolution version of the Max Planck institute Earth System model (MPI-ESM1.2-HR). *Journal of Advances in Modeling Earth Systems*, *10*(7), 1383–1413. https://doi.org/10.1029/2017MS001217

Penduff, T., Le Sommer, J., Barnier, B., Treguier, A.-M., Molines, J.-M., & Madec, G. (2007). Influence of numerical schemes on current-topography interactions in 1/4° global ocean simulations. *Ocean Science*, *3*(4), 509–524. https://doi.org/10.5194/os-3-509-2007

Quartly, G., de Cuevas, B., & Coward, A. (2013). Mozambique channel eddies in GCMs: A question of resolution and slippage. *Ocean Modelling*, *63*, 56–67. https://doi.org/10.1016/j.ocemod.2012.12.011

Rahmstorf, S., & Willebrand, J. (1995). The role of temperature feedback in stabilizing the thermohaline circulation. *Journal of Physical Oceanography*, *25*(5), 787–805. https://doi.org/10.1175/1520-0485(1995)025⟨0787:TROTFI⟩2.0.CO;2

Rayner, N. A., Parker, D. E., Horton, E. B., Folland, C. K., Alexander, L. V., Rowell, D. P., et al. (2003). Global analyses of sea surface temperature, sea ice, and night marine air temperature since the late nineteenth century. *Journal of Geophysical Research*, *108*(D14). https://doi.org/10.1029/2002JD002670

Reick, C. H., Raddatz, T., Brovkin, V., & Gayler, V. (2013). Representation of natural and anthropogenic land cover change in MPI-ESM. *Journal of Advances in Modeling Earth Systems*, *5*(3), 459–482. https://doi.org/10.1002/jame.20022

Reintges, A., Latif, M., Bordbar, M. H., & Park, W. (2020). Wind stress-induced multiyear predictability of annual extratropical North Atlantic sea surface temperature anomalies. *Geophysical Research Letters*, *47*(14), e2020GL087031. https://doi.org/10.1029/2020GL087031

Rieck, J. K., Böning, C. W., & Getzlaff, K. (2019). The nature of eddy kinetic energy in the Labrador Sea: Different types of mesoscale eddies, their temporal variability, and impact on deep convection. *Journal of Physical Oceanography*, *49*(8), 2075–2094. https://doi.org/10.1175/JPO-D-18-0243.1

Roberts, C. D., Waters, J., Peterson, K. A., Palmer, M. D., McCarthy, G. D., Frajka-Williams, E., et al. (2013). Atmosphere drives recent interannual variability of the Atlantic meridional overturning circulation at 26.5°N. *Geophysical Research Letters*, *40*(19), 5164–5170. https://doi.org/10.1002/grl.50930

Robson, J., Sutton, R., Lohmann, K., Smith, D., & Palmer, M. D. (2012). Causes of the rapid warming of the North Atlantic Ocean in the mid-1990s. *Journal of Climate*, *25*(12), 4116–4134. https://doi.org/10.1175/JCLI-D-11-00443.1

Schulzki, T., Harlaß, J., Schwarzkopf, F. U., & Biastoch, A. (2022). Toward ocean hindcasts in earth system models: AMOC variability in a partially coupled model at eddying resolution [Dataset]. GEOMAR Helmholtz Centre for Ocean Research Kiel. https://hdl.handle.net/20.500.12085/57ea9d04-2bd4-4a27-8994-3e19982731bd

Schwarzkopf, F. U., Biastoch, A., Böning, C. W., Chanut, J., Durgadoo, J. V., Getzlaff, K., et al. (2019). The INALT family—A set of high-resolution nests for the Agulhas current system within global NEMO ocean/sea-ice configurations. *Geoscientific Model Development*, *12*(7), 3329–3355. https://doi.org/10.5194/gmd-12-3329-2019

Stevens, B., Giorgetta, M., Esch, M., Mauritsen, T., Crueger, T., Rast, S., et al. (2013). Atmospheric component of the MPI-M Earth System model: ECHAM6. *Journal of Advances in Modeling Earth Systems*, *5*(2), 146–172. https://doi.org/10.1002/jame.20015

Taburet, G., & Pujol, M.-I. (2022). Global Ocean gridded L 4 sea surface heights and derived variables reprocessed copernicus climate Service [Dataset]. Chang. https://doi.org/10.48670/moi-00145

Thoma, M., Gerdes, R., Greatbatch, R. J., & Ding, H. (2015). Partially coupled spin-up of the MPI-ESM: Implementation and first results. *Geoscientific Model Development*, *8*(1), 51–68. https://doi.org/10.5194/gmd-8-51-2015

Tsujino, H., Urakawa, S., Nakano, H., Small, R. J., Kim, W. M., Yeager, S. G., et al. (2018). JRA-55 based surface dataset for driving ocean–sea-ice models (JRA55-do). *Ocean Modelling*, *130*, 79–139. https://doi.org/10.1016/j.ocemod.2018.07.002

Valcke, S. (2013). The OASIS3 coupler: A European climate modelling community software. *Geoscientific Model Development*, *6*(2), 373–388. https://doi.org/10.5194/gmd-6-373-2013

Vancoppenolle, M., Fichefet, T., Goosse, H., Bouillon, S., Madec, G., & Maqueda, M. A. M. (2009). Simulating the mass balance and salinity of Arctic and Antarctic sea ice. 1. Model description and validation. *Ocean Modelling*, *27*(1), 33–53. https://doi.org/10.1016/j.ocemod.2008.10.005

Weijer, W., Cheng, W., Garuba, O. A., Hu, A., & Nadiga, B. T. (2020). CMIP6 models predict significant 21st century decline of the Atlantic Meridional Overturning Circulation. *Geophysical Research Letters*, *47*(12), e2019GL086075. https://doi.org/10.1029/2019GL086075

Yeager, S. (2015). Topographic coupling of the Atlantic overturning and gyre circulations. *Journal of Physical Oceanography*, *45*(5), 1258–1284. https://doi.org/10.1175/JPO-D-14-0100.1

Yeager, S. (2020). The abyssal origins of North Atlantic decadal predictability. *Climate Dynamics*, *55*(7), 2253–2271. https://doi.org/10.1007/s00382-020-05382-4

Zalesak, S. T. (1979). Fully multidimensional flux-corrected transport algorithms for fluids. *Journal of Computational Physics*, *31*(3), 335–362. https://doi.org/10.1016/0021-9991(79)90051-2

Zhang, Q., Chang, P., Yeager, S. G., Danabasoglu, G., & Zhang, S. (2022). Role of sea-surface salinity in simulating historical decadal variations of Atlantic Meridional Overturning Circulation in a coupled climate model. *Geophysical Research Letters*, *49*(4), e2021GL096922. https://doi.org/10.1029/2021GL096922

Zhao, J., & Johns, W. (2014). Wind-forced interannual variability of the Atlantic Meridional Overturning Circulation at 26.5°N. *Journal of Geophysical Research: Oceans*, *119*(4), 2403–2419. https://doi.org/10.1002/2013JC009407

Zweng, M. M., Reagan, J. R., Antonov, J. I., Locarnini, R. A., Mishonov, A. V., Boyer, T. P., et al. (2013). World Ocean Atlas 2013, volume 2: Salinity (NOAA Atlas NESDIS 74).